J|A|C|S
ARTICLES
Published on Web 03/09/2006

Vibrational Markers for the Open-Shell Character of Transition Metal Bis-dithiolenes: An Infrared, Resonance Raman, and Quantum Chemical Study

Taras Petrenko, Kallol Ray, Karl E. Wieghardt, and Frank Neese*

Contribution from the Max Planck Institut für Bioanorganische Chemie, Stiftstrasse 34-36, D-45470 Mülheim an der Ruhr, Germany

Received December 2, 2005; E-mail: neese@mpi-muelheim.mpg.de

Abstract: Transition metal complexes involving the benzene-1,2-dithiol (L^{2-}) and Sellmann's 3,5-di-*tert*-butylbenzene-1,2-dithiol($L^{Bu\ 2-}$) ligands have been studied by UV−vis, infrared (IR), and resonance Raman (rR) spectroscopies. Raman spectra were obtained in resonance with the intervalence charge transfer (IVCT) bands in the near-infrared region and ligand-to-metal charge transfer (LMCT) bands in the near-UV region. Geometry optimization and frequency calculations using density functional theory (DFT) have been performed for $[M(L)_2]^z$ and $[M(L^{Bu})_2]^z$ species (M = Ni, Pd, Pt, Co, Cu, Au, $z = -1$; M = Au, $z = 0$). On the basis of frequency calculations and normal-mode analysis, we have assigned the most important totally symmetric vibrations as well as corresponding overtone and combination bands that appear in rR spectra of compounds $[Ni(L)_2]^{1-}$, $[M(L^{Bu})_2]^{1-}$ (M = Ni, Pt, Co, Cu). Experimental values of dimensionless normal coordinate displacements in excited states have been determined by fitting of rR spectra together with the absorption band shape, based on the time-dependent theory of Heller. Time-dependent density functional theory (TD-DFT) and multireference post-Hartree−Fock ab initio calculations, using the difference dedicated configuration interaction (MR-DDCI) method, were carried out to evaluate dimensionless normal coordinate displacements quantum chemically. The calculations show encouraging agreement with the experimental values. The large distortions along several normal modes led to significant vibronic broadening of IVCT and LMCT bands, and the broadening was accounted for in the deconvolution of the absorption spectra. The presence of an intense rR band around ~1100 cm^{-1} was found to be a reliable marker for the presence of sulfur-based radicals.

1. Introduction

Dithiolene transition metal complexes are of long-standing interest in inorganic chemistry due to their fascinating physical properties and electronic structures. Over the last 40 years, numerous metallodithiolenes (which, depending on the choice of the transition metal and the nature of the dithiolenes, possess lumophoric,[1] magnetic,[2] and conducting[3] properties) have been synthesized. The biological significance of transition metal dithiolenes lies in their ability to catalyze a variety of formal oxygen transfer reactions at the active sites of pyranopterin molybdenum and tungsten enzymes[4] and in specific model systems.[5] However, the understanding of enzymatic reaction mechanisms or design of new functional materials should be based on a thorough understanding of the electronic structures of such compounds. In this respect, an intensely debated question is whether dithiolene ligands can exist as radicals or diradicals.[6]

(1) (a) Biro, D. A.; Sharma, D. K.; Langford, C. H. *J. Indian Chem. Soc.* **1992**, *69*, 413. (b) Cummings, S. D.; Eisenberg, R. *Inorg. Chem.* **1995**, *34*, 2007. (c) Cummings, S. D.; Eisenberg, R. *Inorg. Chem.* **1995**, *34*, 3396. (d) Cummings, S. D.; Eisenberg, R. *J. Am. Chem. Soc.* **1996**, *118*, 1949. (e) Paw, W.; Cummings, S. D.; Mansour, M. A.; Connick, W. B.; Geiger, D. K.; Eisenberg, R. *Coord. Chem. Rev.* **1998**, *171*, 125. (f) VanHouten, K. A.; Heath, D. C.; Barringer, C. A.; Rheingold, A. L.; Pilato, R. S. *Inorg. Chem.* **1998**, *37*, 4647. (g) Rau, S.; Buttner, T.; Temme, C.; Ruben, M.; Gorls, H.; Walther, D.; Duati, M.; Fanni, S.; Vos, J. G. *Inorg. Chem.* **2000**, *39*, 1621.

(2) (a) Fourmigue, M.; Domercq, B. *Actual. Chim.* **1998**, 9. (b) Fourmigue, M.; Lenoir, C.; Coulton, C.; Guyon, F.; Amadraut, J. *Inorg. Chem.* **1995**, *34*, 4979. (c) DaGama, V.; Bello, D.; Santos, I. C.; Henriques, R. T. *Mol. Cryst. Liq. Cryst. Sci. Technol., Sect. A* **1997**, *306*, 17. (d) Livage, C.; Fourmigue, M.; Batail, P.; Canadel, E.; Coulon, C. *Bull. Soc. Chim. Fr.* **1993**, *130*, 761. (e) Noh, D. Y.; Mizuno, M.; Choy, J. H. *Synth. Met.* **1997**, *86*, 1837. (f) Akutsu, H.; Arai, E.; Kobayasachi, H.; Tanaka, H.; Kobayasachi, A.; Cassoux, P. *J. Am. Chem. Soc.* **1997**, *119*, 12681. (g) Kobayasachi, H.; Sato, A.; Arai, E.; Akutsu, H.; Kobayasachi, A.; Cassoux, P. *J. Am. Chem. Soc.* **1997**, *119*, 12392. (h) Pulloen, A. E.; Pokhodnya, K. I.; Faulmann, C.; Tokumoto, M.; Cassoux, P. *Synth. Met.* **1991**, *42*, 2191.

(3) (a) Cassoux, P.; Valade, L.; Kobayashi, H.; Kobayashi, A.; Clark, R. A.; Underhill, A. E. *Coord. Chem. Rev.* **1991**, *110*, 115. (b) Doidgeharrison, S.; Howie, R. W.; Irvine, J. T. S.; Spencer, G.; Wardell, J. L. *J. Organomet. Chem.* **1991**, *414*, C5. (c) Doublet, M. L.; Canadell, E.; Garreau, B.; Legros, J. P.; Brossard, P.; Cassoux, P.; Pouget, J. P. *J. Phys.: Condens. Matter* **1995**, *7*, 4673. (d) Kato, R.; Kashimura, Y.; Aonuma, S.; Hanasaki, N.; Tajima, H. *Solid State Commun.* **1998**, *105*, 561. (e) Miyazaki, T.; Ohno, T. *Phys. Rev. B, Condens. Matter* **1999**, *59*, R5269.

(4) (a) Enroth, C.; Eger, B. T.; Okamoto, K.; Nishino, T.; Nishino, T.; Pai, E. F. *Proc. Natl. Acad. Sci. U.S.A.* **2000**, *272*, 1599. (b) Bray, R. C.; Malmström, B. G.; Vänngard, T. *Biochem. J.* **1959**, *73*, 193. (c) Hille, R.; Nishino, T. *FASEB J.* **1995**, *9*, 995. (d) Hille, R. *Chem. Rev.* **1996**, *96*, 2757. (e) Campbell, W. *Plant Physiol.* **1996**, *111*, 355. (f) Solomonson, L. P.; Barber, M. P. *Plant Mol. Biol.* **1990**, *41*, 225. (g) Li, H.-L.; Temple, C.; Rajagopalan, K. V.; Schindfelin, H. *J. Am. Chem. Soc.* **2000**, *122*, 7673. (h) Cammack, R.; Weiner, J. H. *Biochemistry* **1990**, *29*, 8410. (i) Ellis, P.; Conrads, T.; Hille, R.; Kuhn, P. *Structure* **2001**, *9*, 125. (j) Anderson, G. L.; Williams, J.; Hille, R. *J. Biol. Chem.* **1992**, *267*, 23674. (k) Mukund, S.; Adams, M. W. W. *J. Biol. Chem.* **1991**, *266*, 14208.

(5) (a) Lim, B. S.; Sung, K. M.; Holm, R. H. *J. Am. Chem. Soc.* **2000**, *122*, 7410. (b) Lim, B. S.; Holm, R. H. *J. Am. Chem. Soc.* **2001**, *123*, 1920. (c) Lim, B. S.; Donahue, J. P.; Holm, R. H. *Inorg. Chem.* **2000**, *39*, 263. (d) Sung, K. M.; Holm, R. H. *Inorg. Chem.* **2001**, *40*, 4518. (e) Sung, K. M.; Holm, R. H. *J. Am. Chem. Soc.* **2001**, *123*, 1931.

10.1021/ja0578451 CCC: $33.50

In such "noninnocent" complexes, the oxidation and spin state of the central metal are ambiguous and difficult to determine experimentally. The situation is further complicated if an electron-transfer series of bis-dithiolene transition metal complexes such as $[MS_4]^{2-}$, $[MS_4]^{1-}$, and $[MS_4]^0$ is considered where the members possess almost identical geometries and are interrelated by reversible one-electron steps. Thus, the study of the electron distribution in metal dithiolenes has been of particular interest to physical inorganic chemists. In fact, EPR spectra,[7] electronic spectra,[6b,7d,8] resonance Raman (rR) spectra,[9,10] and Mössbauer spectra[11] have been studied, and semiempirical MO,[12] density functional theory (DFT),[13] and ab initio[7d,14] calculations have been performed on metal dithiolenes.

Recently, Solomon and co-workers[15] have used sulfur K-edge X-ray absorption spectroscopy (XAS) to probe the ground-state wave functions of the $[Ni(Me_2C_2S_2)_2]^{2-/1-/0}$ complexes. A transition dipole integral for the dithiolene sulfur was determined, and it was concluded that the acceptor orbitals of the $[Ni(Me_2C_2S_2)_2]^{2-/1-/0}$ series possess greater than 50% sulfur character. Therefore, the bonding description of $[Ni(Me_2C_2S_2)_2]^{2-/1-/0}$ is said to be "inverted", with dithiolene valence orbitals lying at higher energy than the Ni d-orbital manifold. This exemplifies the noninnocent behavior of dithiolene ligands in many metallodithiolene complexes.

As for vibrational spectra, building upon earlier partial IR assignments,[16] the IR studies of $[Ni(S_2C_2R_2)_2]^z$ complexes, where R = H, Ph, CF_3, or CN and $z = 0$, 1−, or 2−, conducted by Nakamoto and Schläpfer,[17] constitute the most comprehensive vibrational study of any series of metal dithiolenes. For each complex, detailed assignments were reported on the basis of $^{58}Ni/^{62}Ni$ isotope shifts and normal coordinate analysis using the **GF** matrix method together with Urey−Bradley force fields. The C−C stretching frequency (1394−1594 cm^{-1}) was shown to be the most convenient indicator of the redox state of the dithiolene ligand since this mode is not extensively mixed with other vibrations. In contrast, the C−S (800−900 cm^{-1}) and Ni−S (300−400 cm^{-1}) stretches were found to be extensively coupled with the in-plane deformation modes, rendering the absolute frequencies to limited value, particularly for comparisons between different complexes. Due to the increasing energy of the C−C stretches with increasing negative charge on the complexes, all redox processes were argued to be predominantly ligand-centered. However, Holm and co-workers have argued that similar variations in the ν(C−C) stretches would also be expected for metal-based redox processes.[18] Predominantly ligand-based redox processes have also been inferred for the electron-transfer series $[M(S_2C_2(CN)_2]^{1-,2-,3-}$ by monitoring the ν(C≡N) frequency in IR spectroelectrochemical studies.[19] However, in the absence of other data, it is difficult to settle the issue of metal-centered versus ligand-centered oxidation from IR studies alone.

rR spectroscopy can selectively probe the vibrational modes of compounds that are in resonance with a given electronic transition. In the resonance region, those fundamentals that reflect the change in geometry, when converting the molecule from its ground to excited state (Franck−Condon allowed), or those that are able to vibronically couple the resonant excited state to some other electronic state, with a different transition moment (Herzberg−Teller allowed), will be strongly enhanced.[20] The former effect is restricted to totally symmetric modes and electric dipole allowed electronic transitions, whereas the latter is also allowed for nontotally symmetric modes and weakly allowed or forbidden electronic transitions. The electronic spectra of the dithiolene complexes are all dominated by intense allowed optical transitions in the visible and near-IR spectral regions,[7d,11c,21] and hence it is expected that the Franck−Condon mechanism will be dominant in enhancing totally symmetric modes.[22] Thus, the correct identification of the vibrational modes showing rR enhancement will aid in the assignment of the electronic transitions and vice versa. Moreover, the excited-state distortion patterns, deduced from a thorough analysis of the rR intensities, reflect the electronic and geometric structure of the electronic ground and excited states.

The potential use of vibrational spectroscopy in characterizing the extent of π delocalization and metal- versus ligand-based redox chemistry in transition metal dithiolenes clearly indicates a need for parallel IR and rR studies together with the rationalization of their force fields developed using DFT and normal-mode calculations. This approach is required for meaningful assignment and interpretation of modes involving M−S and C−S stretchings, in particular, because these modes are extensively mixed with stretching and deformation modes of the dithiolene ring and substituents. However, relatively few[6f] of the published vibrational studies of the dithiolene complexes report both IR and rR data, and consequently, the assignments

(6) (a) Schrauzer, G. N. *Transition Met. Chem.* **1968**, *4*, 299. (b) McCleverty, J. A. *Prog. Inorg. Chem.* **1968**, *10*, 49. (c) Holm, R. H.; O'Connor, M. J. *Prog. Inorg. Chem.* **1971**, *14*, 241. (d) Eisenberg, R. *Prog. Inorg. Chem.* **1970**, *12*, 295. (e) Gray, H. B. *Transition Met. Chem.* **1965**, *1*, 240. (f) Johnson, M. K. Vibrational Spectra of Dithiolene Complexes. In *Dithiolene Chemistry: Synthesis, Properties, and applications*; Stiefel, E. I., Ed.; Progress in Inorganic Chemistry; Wiley: Hoboken, NJ, 2004; Vol. 52.

(7) (a) Schmitt, R. D.; Maki, A. H. *J. Am. Chem. Soc.* **1968**, *90*, 2288. (b) Maki, A. H.; Edelstein, N.; Davison, A.; Holm, R. H. *J. Am. Chem. Soc.* **1964**, *86*, 4580. (c) Huyett, J. E.; Choudhury, S. B.; Eichhorn, D. M.; Bryngelson, P. A.; Maroney, M. J.; Hoffman, B. M. *Inorg. Chem.* **1998**, *37*, 1361. (d) Ray, K.; Weyhermüller, T.; Neese, F.; Wieghardt, K. *Inorg. Chem.* **2005**, *44*, 5345.

(8) Ray, K.; Begum, A.; Weyhermüller, T.; Piligkos, S.; Neese, F.; Wieghardt, K. *J. Am. Chem. Soc.* **2005**, *127*, 4403.

(9) (a) Clark, R. J. H.; Turtle, P. C. S. *J. Chem. Soc., Dalton Trans.* **1977**, 2142. (b) Clark, R. J. H.; Turtle, P. C. S. *J. Chem. Soc., Dalton Trans.* **1978**, 1714.

(10) Wootton, J. L.; Zink, J. I. *J. Phys. Chem.* **1995**, *99*, 7251.

(11) (a) Sellmann, D.; Geck, M.; Knoch, F.; Ritter, G.; Dengler, J. *J. Am. Chem. Soc.* **1991**, *113*, 3819. (b) Sellmann, D.; Kleine-Kleffmann, U.; Zapf, L.; Huttner, G.; Zsolnai, L. *J. Organomet. Chem.* **1984**, *263*, 321. (c) Ray, K.; Bill, E.; Weyhermüller, T.; Wieghardt, K. *J. Am. Chem. Soc.* **2005**, *127*, 5641.

(12) (a) Schrauzer, G. N.; Mayweg, V. P. *J. Am. Chem. Soc.* **1965**, *87*, 3585. (b) Shupack, S. I.; Billig, E.; Clark, R. J. H.; Williams, R.; Gray, H. B. *J. Am. Chem. Soc.* **1964**, *86*, 4594. (c) Viste, A.; Gray, H. B. *Inorg. Chem.* **1964**, *3*, 1113. (d) Ballhausen, C. J.; Gray, H. B. Ibid, **1962**, *1*, 111.

(13) (a) Lim, B. S.; Fomitchev, D. V.; Holm, R. H. *Inorg. Chem.* **2001**, *40*, 4257. (b) Bachler, V.; Olbrich, G.; Neese, F.; Wieghardt, K. *Inorg. Chem.* **2002**, *41*, 4179. (c) Ribas, X.; Dias, J. C.; Morgado, J.; Wurst, K.; Molins, E.; Ruiz, E.; Almeida, M.; Veciana, J.; Rovira, C. *Chem.−Eur. J.* **2004**, *10*, 1691.

(14) Schiødt, N. C.; Sommer-Larsen, P.; Bjørnholm, T.; Nielsen, M. F.; Larsen, J.; Bechgaard, K. *Inorg. Chem.* **1995**, *34*, 3688.

(15) Szilygyi, R. K.; Lim, B. S.; Glaser, T.; Holm, R. H.; Hedman, B.; Hodgson, K. O.; Solomon, E. I. *J. Am. Chem. Soc.* **2003**, *125*, 9158.

(16) (a) Adams, D. M.; Cornell, J. B. *J. Chem. Soc. A* **1968**, 1299. (b) Schrauzer, G. N.; Mayweg, V. P. *J. Am. Chem. Soc.* **1965**, *87*, 3585. (c) Schrauzer, G. N.; Mayweg, V. P. *J. Am. Chem. Soc.* **1965**, *87*, 1483.

(17) Nakamoto, K.; Schläpfer, C. W. *Inorg. Chem.* **1975**, *14*, 1338.

(18) Davison, A.; Edelstein, N.; Holm, R. H.; Maki, A. H. *Inorg. Chem.* **1964**, *3*, 814.

(19) Best, S. P.; Ciniawsky, S. A.; Clark, R. J. H.; McQueen, R. C. S. *J. Chem. Soc., Dalton Trans.* **1993**, 2267.

(20) (a) Albrecht, A. C. *J. Chem. Phys.* **1961**, *34*, 1476. (b) Tang, J.; Albrecht, A. C. In *Raman Spectroscopy, Theory and Practice*; Szymanski, H. A. Ed.; Plenum Press: New York, 1970; p 33.

(21) Ray, K.; Weyhermüller, T.; Goossens, A.; Crajé, M. W. J.; Wieghardt, K. *Inorg. Chem.* **2003**, *42*, 4082.

(22) Czernuszewicz, R. S.; Spiro, T. G. In *Inorganic Electronic Structure and Spectroscopy*; Solomon, E. I., Lever, A. B. P., Eds.; Wiley-Interscience: New York, 1999; Vol. I, p 353.

of M−S and C−S vibrational modes are incomplete and of limited utility for assessing trends in dithiolene ligation. For the monoanionic paramagnetic $[MS_4]^{1-}$ complexes,[7d] in particular, no detailed rR studies have been published. Such a study may be of further relevance for the understanding of the complex rR spectra of enzymes containing the Mo- or W-pyranopterin cofactors. The most detailed studies available have been conducted for the DMSO reductase family[23] and specific model systems.[24]

In a series of previous publications[7d,8,11c,21] from our group, we have elucidated in detail the electronic structures of the transition metal complexes involving the benzene-1,2-dithiolate (L refers to the dianionic closed shell ligand throughout this article) and Sellmann's 3,5-di-*tert*-butylbenzene-1,2-dithiolate-$(L^{Bu})^{2-}$ ligands by experimental, DFT, and correlated ab initio methods. It has been demonstrated that the ligands in such complexes readily undergo one-electron oxidation, yielding *S*,*S*′-coordinated dithiobenzosemiquinonate (*S*-centered) radical(1−) ions (the monoradical state of the ligand is denoted as $L^{\bullet}$ throughout this article). Spectroscopic markers[7d,8,11c,21] for such radical ions have been assigned as follows: (i) the presence of intense ligand-to-ligand charge-transfer bands in the near-infrared region; (ii) for complexes involving the (L^{Bu}) ligands, an intense IR band at ∼1100 cm^{-1}. Structural parameters were shown to have only limited value for the identification of the redox state of the benzene-1,2-dithiolate ligands in a given complex.

In this article, we report a detailed analysis of the vibrational spectra of a series of bis-benzenedithiolene transition metal complexes by a combination of the IR and rR spectral studies. Quantum mechanical studies have also been performed to analyze the origin of the IR band at ∼1100 cm^{-1}. In particular, we demonstrate a methodology to directly predict the rR intensities which greatly aids in the interpretation of the experimental results. The results described in section 3 indicate that IR intensities have to be viewed with caution since they strongly depend on substituent effects and the intensity mechanism is indirect. By contrast, the corresponding totally symmetric rR bands, also observed around ∼1100 cm^{-1}, have an electronic origin related to the radical character of the dithiolene ligands, and are hence a more reliable vibrational indicator of the open-shell character.

2. Materials and Methods

2.1. Synthesis and Characterization of Complexes. The synthesis of the following complexes has been described in the literature: $[Co(L^{Bu})_2][(N(n\text{-}Bu)_4]$,[8] $[Ni(L^{Bu})(L^{Bu\bullet})][(N(n\text{-}Bu)_4]$,[7d] $[Ni(L)(L^{\bullet})][(N(n\text{-}Bu)_4]$,[7d] $[Ni(L^{Bu})_2][(N(n\text{-}Bu)_4]_2$,[7d] $[Pd(L^{Bu})(L^{Bu\bullet})][(N(n\text{-}Bu)_4]$,[7d] $[Pd(L^{Bu})_2][(N(n\text{-}Bu)_4]_2$,[7d] $[Pt(L^{Bu})(L^{Bu\bullet})][(N(n\text{-}Bu)_4]$,[7d] $[Pt(L^{Bu})_2][(N(n\text{-}Bu)_4]_2$,[7d] $[Au(L^{Bu})(L^{Bu\bullet})]$,[21] $[Au(L^{Bu})_2][(N(n\text{-}Bu)_4]$,[21] and $[Cu^{III}(L^{Bu})_2]^{1-}$.[7d] The infrared spectra of the complexes were measured on a Perkin-Elmer FT-IR spectrophotometer 2000. Powder IR spectra were measured on KBr pellets with a spectral resolution of 2 cm^{-1}. UV−vis spectra were recorded on an HP 8452A diode array spectrophotometer, or on a PE Lambda 19 spectrophotometer. Near-IR measurements were performed on a Lambda 19 spectrophotometer, using Hellma Quartz Suprasil 3000 cells.

2.2. Resonance Raman Measurements. Resonance Raman spectra in the red and near-IR spectral ranges were obtained using a Ti:Sa laser (Spectra Physics, model 3900S) that operates in the TEM00 transverse mode regime and provides variable energy laser excitation. An Ar^+ ion laser (Spectra Physics, model BeamLok 2060-7SR) with an output power around 10 W was used as a pump. A gold grating optimized for near-IR region (Edmund Optics, 830 grooves/mm, maximum efficiency at 800 nm) together with a manually adjustable slit was used to eliminate laser sidebands. The incident power on the sample was in the range 30−200 mW. No significant degradation of sample integrity was observed during the experiments. In the UV and visible spectral regions, a series of lines from an Ar^+/Kr^+ ion laser (Spectra Physics, model BeamLok 2060-6S) with incident power 5−30 mW was employed as an excitation source. In this case, narrow band-pass interference filters (Edmund Optics) in the range of 350−676 nm were used to eliminate laser sidebands. The scattered light was dispersed with a triple monochromator (Acton Research, TriplePro) equipped with 600, 1200, 2400 grooves/mm holographic gratings. The focal length was 300 mm for both monochromators in subtractive stage and 500 mm for the monochromator in the final dispersion stage. A liquid nitrogen cooled CCD detector (Roper Scientific, SPEC10-LN) with a 400 × 1340 array of pixels was used for detection.

rR data were obtained at ∼77 K for concentrated frozen sample solutions (optical density ∼10−50 cm^{-1}) in quartz tubes commonly used for electron paramagnetic resonance measurements. A 180° backscattering geometry was employed. A polarization scrambler was placed in front of the entrance slit of the spectrometer to account for the polarization sensitivity of the gratings. The entrance and exit slits were of the same width, which varied between 50 and 200 μm. The corresponding spectral slit width was in a range of 2.8−12 cm^{-1}. The slit width was chosen to ensure maximum signal and minimal spectral distortion. The spectra, measured with an acquisition time of 10−1000 s, were linearized in wavenumbers, yielding an increment between 0.1 and 1.0 cm^{-1}. Several spectra (up to three) covering different but overlapping ranges were normalized for acquisition time and combined to give the raw rR spectra. A smooth background was obtained as a linear interpolation between the points of supposedly zero signal and was subtracted from the raw data. We have deliberately used samples of very high optical density, which was chosen high enough to essentially suppress the Raman peaks of the solvent used. The rR spectra have been corrected for self-absorption using the appropriate equations for the 180° backscattering geometry.[25] However, owing to the broadness of the absorption bands studied, the self-absorption correction did not lead to noticeable changes of the rR spectra for the range of excitation wavelengths used. Raman shifts were calibrated using the Raman peaks of Na_2SO_4 (993 cm^{-1}) and solvent peaks (CH_2Cl_2; peaks at 294, 702, 1160, 1407 cm^{-1}) as internal standards.

2.3. Electronic Structure Calculations. The geometry optimization and frequency calculations were performed with the Gaussian03[26] program suite at the BP86 level[27] of density functional theory. This functional has shown excellent agreement between calculated harmonic frequencies and observed fundamental vibrational peaks. This agreement has been partially attributed to a cancellation of a neglect of anharmonicity and a slight overestimation of the harmonic frequencies.[28] The all-electron Gaussian basis sets used were those reported by the Ahlrichs group.[29] For sulfur and ligand carbon atoms, the TZVP basis

(23) (a) Garton, S. D.; Hilton, J. C.; Oku, H.; Crouse, B. R.; Rajagopalan, K. V.; Johnson, M. K. *J. Am. Chem. Soc.* **1997**, *119*, 12906. (b) Garton, S. D.; Temple, C. A.; Dhawan, I. K.; Barber, M. J.; Rajagopalan, K. V.; Johnson, M. K. *J. Biol. Chem.* **2000**, *275*, 6798. (c) Johnson, M. K.; Garton, S. D.; Oku, H. *J. Biol. Inorg. Chem.* **1997**, *2*, 797.
(24) (a) McNaughton R. L.; Tipton, A. A.; Rubie, N. D.; Conry, R. R.; Kirk, M. L. *Inorg. Chem.* **2000**, *37*, 5697. (b) Inscore, F. E.; MacNaughton, R.; Westcott, B. L.; Helton, M. E.; Jones, R.; Dhawan, I. K.; Enemark, J. H.; Kirk, M. L. *Inorg. Chem.* **1999**, *38*, 1401.
(25) Shriver, D. F.; Dunn, J. B. R. *Appl. Spectrosc.* **1974**, *28*, 319.
(26) Frisch, M. J.; et al. *Gaussian 03, revision B.01*; Gaussian, Inc.: Pittsburgh, PA, 2003.
(27) (a) Becke, A. D. *Phys. Rev. A.* **1988**, *38*, 3098. (b) Perdew, J. P. *Phys. Rev. B* **1986**, 33, 8822.
(28) Neugebauer, J.; Hess, B. *J. Chem. Phys.* **2003**, *118*, 7215.

set was applied. These bases are of triple-ζ quality for the valence electrons and augmented by one set of polarization functions. For hydrogen atoms in ring and carbon atoms in the substituent groups that are adjacent to the carbon ring, the TZV basis set was employed. The remaining atoms in substituent groups (hydrogens and carbons) were described by a split-valence (SV) basis set that is of double-ζ quality. Stuttgart/Dresden ECPs were applied to metal atoms together with the corresponding basis sets.[30] The auxiliary basis sets used to fit electron density in the resolution of identity (RI)[31] approximation were automatically generated from AO basis. The geometry optimization preceding frequency calculation was carried out using the Berny algorithm in redundant internal coordinates with imposition of symmetry constraints. Vibrational frequencies for unsubstituted complexes $[M(L)_2]^{1-}$ were calculated analytically, while for substituted species $[M(L^{Bu})_2]^{1-}$, they were calculated by numerical differentiation of analytic gradients with a displacement value of 0.001 Å. Calculated frequencies have shown that all structures reported here are indeed minima on the potential energy surface. Calculated frequencies of the totally symmetric modes for the complexes are in good agreement with the experiments, with a deviation from experiment ≤ 30 cm^{-1}.

The calculated in-plane vibrations for unsubstituted complexes of D_{2h} symmetry have been classified by the percentage contribution to pure metal−sulfur (P_{MS}) and carbon−sulfur (P_{CS}) stretches. The value P_{12}^i, characterizing partitioning of the bond stretch between atoms 1 and 2 among $(3N-6)$ normal modes, is defined in the following way:

$$P_{AB}^i = (\mathbf{D}_{AB}\mathbf{Q}^i)^2 \quad i \in [1,3N-6] \tag{1.1}$$

where all the vectors are defined in Cartesian mass-weighted coordinates, $\mathbf{D}_{AB}$ is a $(3N-6)$-component unit vector that represents the purely diatomic stretching normal mode between atoms A and B, and $\mathbf{Q}^i$ is the ith molecular normal mode. Therefore, one can easily see that $\sum_{i=1}^{3N-6} P_{AB}^i = 1$.

To predict rR intensities from quantum chemistry, it is necessary to map out the shape of the ground- and excited-state potential energy surfaces (PES) in some detail. In the present work, a three-point parabolic fit was constructed on the basis of the calculated total energies at the ground-state equilibrium geometry and structures that were displaced along normal modes. The compositions of the normal modes were taken from frequency calculations performed at the BP86/TZVP level of theory. Excited-state displacements were calculated for a number of selected modes with the largest rR enhancement. Subsequently, these displacements were used to construct absorption band shapes based on the time dependent theory of Heller.[32] Potential energy surface scan calculations were performed with the electronic structure program, ORCA.[33] For metal and sulfur carbon atoms, the TZVP[29] basis set was applied and for the remaining atoms we used the split-valence polarized SVP[29] basis set. The calculations of excited-state energies within the TD-DFT approach were done at the BP86[27] level to keep the consistency with the ground-state frequency calculations. For open-shell systems, the TD-DFT formalism does not provide the proper spin couplings for the description of the excited states due to restrictions imposed by the single determinantal reference wave function.[34] This drawback is noteworthy for transitions with doublet ground states involving electron promotion from a doubly occupied MO to an empty MO. In this case, there are two singly excited spin-doublet configuration state functions (CSF), which are represented by linear combination of normalized Slater determinants with $(n-1)$ doubly and three singly occupied MOs:[35]

$$|I_i^a \tfrac{1}{2}\tfrac{1}{2}\rangle = \frac{1}{\sqrt{2}}\{|\psi_1\bar{\psi}_1...\psi_i\bar{\psi}_a...\psi_n\bar{\psi}_n\psi_o| + |\psi_1\bar{\psi}_1...\psi_a\bar{\psi}_i...\psi_n\bar{\psi}_n\psi_o|\} \tag{1}$$

$$|II_i^a \tfrac{1}{2}\tfrac{1}{2}\rangle = \frac{1}{\sqrt{6}}\{2|\psi_1\bar{\psi}_1...\psi_i\psi_a...\psi_n\bar{\psi}_n\bar{\psi}_o| - |\psi_1\bar{\psi}_1...\psi_a\bar{\psi}_i...\psi_n\bar{\psi}_n\psi_o| + |\psi_1\bar{\psi}_1...\psi_i\bar{\psi}_a...\psi_n\bar{\psi}_n\psi_o|\} \tag{2}$$

It is evident that the second spin coupling represents a so-called "trip-doublet",[36] where a triplet excitation out of the closed shell subsystem is coupled to a spin-flip in the SOMO. It involves the doubly excited determinant $|\psi_1\bar{\psi}_1...\psi_i\psi_a...\psi_n\bar{\psi}_n\bar{\psi}_o|$, which cannot be described by TD-DFT treatment. Therefore, to provide an appropriate theoretical treatment of the excited states involving electron promotion from the doubly occupied MOs to empty MOs, multireference configuration interaction (MR-CI) methods were applied. In these calculations, CSFs of the correct total spin were constructed as a many electron basis. Integrals over four MOs were approximated with the RI approximation.[37,38] In individually selecting MR-CI calculations, a test configuration was kept if its perturbation energy $H_{I0}^2/\Delta E$ was larger than a threshold T_{sel} (H_{I0} is the CI matrix element between the test configuration and muticonfigurational order wave function, and ΔE is the energy difference calculated with the Möller−Plesset (MP) 0th order Hamiltonian). The values reported in the main body of the article were obtained with $T_{sel} = 10^{-6}$ Eh, which leads to well-converged results. The energetic effects of unselected CSFs were estimated by second-order Rayleigh−Schrödinger theory using MP partitioning. We have explored the difference dedicated CI (DDCI) approach of Malrieu and co-workers[39] in the DDCI2 variant. For each compound, the smallest reference space containing the leading configurations for all states of interest was used. Thus, we chose a three-level restricted active space (Olsen et al.;[40] for the notation, see ref 38) RAS(9:41/1/11) to explore the $^2B_{1u}(1b_{1u} \rightarrow 2b_{2g})$,$^2A_u(1a_u \rightarrow 2b_{2g})$, and $^2B_{3u}(1a_u \rightarrow 1b_{1g})$ excited states of $[Ni^{II}(L)(L^{\bullet})]^{1-}$, RAS(10:51/0/11) for $^1B_{1u}(1a_u \rightarrow 1b_{1g})$ state of $[Cu^{III}(L)_2]^{1-}$, and RAS (8:31/0/23) for $^3B_{2u}(1b_{1u} \rightarrow 2b_{2g})$ and $^3B_{3u}(1a_u \rightarrow 2b_{2g})$ states of $[Co(L)_2]^{1-}$ (see section 3). The molecular orbitals have been obtained from Kohn−Sham restricted open shell (for $[Ni^{II}(L)(L^{\bullet})]^{1-}$ and $[Co(L)_2]^{1-}$) and closed shell (for $[Cu^{III}(L)_2]^{1-}$) DFT calculations using the BP86 functional.[27]

3. Results and Analysis

3.1. Electronic States of Transition Metal Dithiolenes. The electronic structures of $[M(L)_2]^z$ complexes, where M = Ni, Pd, Pt, Co, and Cu and $z = -1$, and where M = Au for $z = 0$, were previously considered in detail.[7d,8,11c,21] It has been shown that the electronic spectra of such complexes can be well explained in terms of a simplified MO picture (Figure 1). While the a_u and b_{1u} orbitals in Figure 1 represent pure ligand orbitals, the $2b_{2g}$, $2b_{3g}$, and the $1b_{1g}$ orbitals are shown to be delocalized over the metal and ligand orbitals. The question of metal versus

(29) (a) Schäfer, A.; Horn, H.; Ahlrichs, R. *J. Chem. Phys.* **1992**, *97*, 2571. (b) Schäfer, A.; Huber, C.; Ahlrichs, R. *J. Chem. Phys.* **1994**, *100*, 5829.
(30) Dolg, M.; Wedig, U.; Stoll, H.; Preus, H. *J. Chem. Phys.* **1987**, *86*, 866.
(31) (a) Baerends, E. J.; Ellis, D. E.; Ros, P. *Chem. Phys.* **1973**, *2*, 41. (b) Dunlap, B. I.; Conolly, J. W. D.; Sabin, J. R. *J. Chem. Phys.* **1979**, *78*, 3396. (c) Vahtras, O.; Almlöf, J. E.; Feyereisen, M. W. *Chem. Phys. Lett.* **1993**, *213*, 514.
(32) Tannor, D. J.; Heller, E. J. *J. Chem. Phys.* **1982**, *77*, 202.
(33) Neese, F. *Orca: An ab Initio, DFT and Semiempirical Electronic Structure Package*, version 2.4, revision 39; Max-Planck Institut für Bioanorganische Chemie: Mülheim, Germany, August 2005.
(34) Strictly speaking, this discussion applies to spin-unrestricted configuration interaction with single excitations (UCIS). However, the same failures are observed in TD-DFT calculations and are qualitatively well explained in the UCIS language.
(35) Neese, F.; Solomon, E. I. In *Magnetoscience-From Molecules to Materials*; Drillon, M., Miller, J. S., Eds.; Wiley: New York, 2003; Vol. 4, p 345.
(36) (a) Ake, R. L.; Gouterman, M. *Theor. Chim. Acta* **1969**, *15*, 20. (b) Stavrev, K.; Zerner, M. C. *Chem. Phys. Lett.* **1995**, *233*, 179.
(37) (a) Grimme, S.; Waletzke, M. *J. Chem. Phys.* **1999**, *111*, 5845. (b) Grimme, S.; Waletzke, M. *Phys. Chem. Chem. Phys.* **2000**, *2*, 2075.
(38) Neese, F. *J. Chem. Phys.* **2003**, *119*, 9428.
(39) Miralles, J.; Castell, O.; Caballol, R.; Malrieu, J. P. *Chem. Phys. Lett.* **1993**, *172*, 33.
(40) Olsen, J; Roos, B. O.; Jörgensen, P.; Jensen, H. J. A. *J. Chem. Phys.* **1988**, *89*, 2185.

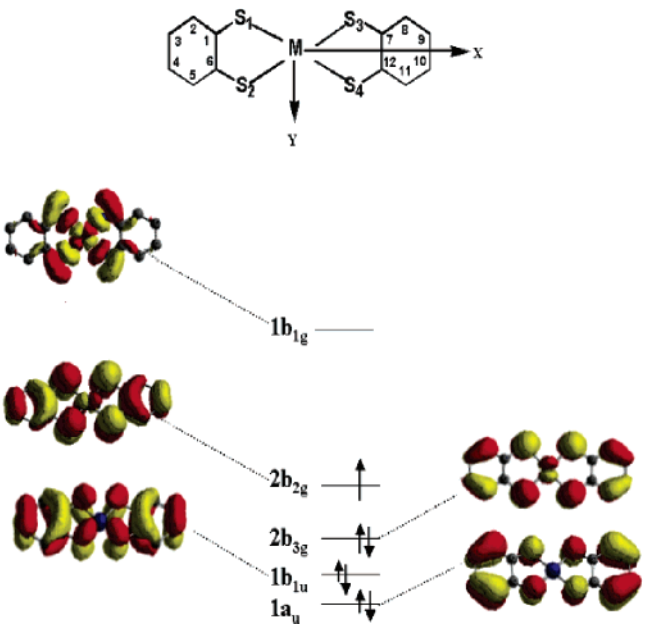

Figure 1. Simplified MO scheme for the $[M^{II}(L)(L^{\bullet})]^{1-}$ (M = Ni, Pd, and Pt) and $[Au^{III}(L)(L^{\bullet})]$ complexes having a spin doublet ground state. For the $[Co(L)_2]^{1-}$ complex, the ground state is spin triplet with the $2b_{3g}$ and $2b_{2g}$ orbitals singly occupied. The corresponding $[Cu^{III}(L)_2]^{1-}$ complex is diamagnetic with the $2b_{2g}$ orbital doubly occupied. Note that throughout the article we refrain from assigning the valence and charge state of the metal and the ligand in ambiguous cases such as $[Co(L)_2]^{1-}$.

ligand oxidation in a series of transition metal dithiolenes has thus been found to be dependent on the extent of delocalization in the redox-active $2b_{2g}$ orbital, which is an antibonding combination of the ligand b_{2g} and the metal d_{xz} orbitals. Its character is mainly controlled by the effective nuclear charge of the central metal ion involved.

In the isoelectronic $[M(L)_2]^{1-}$, where M = Ni, Pd, Pt, and $[Au(L)_2]$ complexes, with an electron configuration of $(1a_u)^2(1b_{1u})^2(2b_{3g})^2(2b_{2g})^1(1b_{1g})^0$, the $2b_{2g}$ orbital is predominantly ligand-based owing to the high effective nuclear charge of the metal. The electronic structures of the complexes[7d] have thus been best denoted as $[M^{II}(L)(L^{\bullet})]^{1-}$ (M = Ni, Pd, and Pt) and $[Au^{III}(L)(L^{\bullet})]$, respectively. The $[Cu(L)_2]^{1-}$ complex, with an electron configuration of $(1a_u)^2(1b_{1u})^2(2b_{3g})^2(2b_{2g})^2(1b_{1g})^0$, is a clear case of $[Cu^{III}(L)_2]^{1-}$.[7d,11c] The corresponding $[Co(L)_2]^{1-}$ complex, with the $(1a_u)^2(1b_{1u})^2(2b_{3g})^1(2b_{2g})^1(1b_{1g})^0$ configuration, has been found to be more subtle.[8] In this case, the $2b_{2g}$ orbital possesses equivalent metal and ligand character, and correspondingly, the electronic structure is best represented by the resonance forms $[Co^{III}(L^{2-})(L^{2-})]^- \leftrightarrow [Co^{II}(L^{\bullet-})(L^{2-})]^- \leftrightarrow [Co^{II}(L^{2-})(L^{\bullet-})]^-$.

Under D_{2h} symmetry assumed for the complexes reported in this article, all the spin and electric dipole allowed transitions, together with the corresponding excited states, are summarized in Table 1. The $1b_{1u} \rightarrow 2b_{2g}$ transition in the $[M(L)(L^{\bullet})]^z$ complexes is predominantly ligand-to-ligand intervalence charge transfer (IVCT) in origin and is assigned to the intense band in the near-IR region.[7d,11c,21] Note that we still refer to this transition as "intervalence charge transfer" despite the fact that our system is class III mixed valence systems where there is no net charge transfer between sites. The $1a_u \rightarrow 1b_{1g}$ transition is a *z*-polarized ligand-to-metal charge transfer (LMCT) transition and is assigned to the experimental charge-transfer band in the UV region.[7d] For the $[Co(L)_2]^{1-}$ complex, the $1b_{1u} \rightarrow 2b_{2g}$ transition has been speculated[8] to have equal IVCT and LMCT characters. This is consistent with its blue shift relative to the $[M(L)_2]^{1-}$ (M = Ni, Pd, Pt) complexes.

Table 1. Spin and Electric Dipole Allowed Transitions Possible in the $[M(L)_2]^z$ (M = Ni, Pd, Pt, $z = -1$; M = Au, $z = 0$), $[Cu^{III}(L)_2]^{1-}$, and $[Co(L)_2]^{1-}$ Complexes Studied in This Article

complex type	ground state	excited states	polarization
$[M^{II}(L)(L^{\bullet})]^{1-}$ (M = Ni, Pd, Pt)	$^2B_{2g} \rightarrow$	$^2B_{1u}(1b_{1u} \rightarrow 2b_{2g})$	X
or		$^2A_u(1a_u \rightarrow 2b_{2g})$	Y
$[Au^{III}(L)(L^{\bullet})]$		$^2B_{3u}(1a_u \rightarrow 1b_{1g})$	Z
$[Cu^{III}(L)_2]^{1-}$	$^1A_g \rightarrow$	$^1B_{1u}(1a_u \rightarrow 1b_{1g})$	Z
$[Co(L)_2]^{1-}$	$^3B_{1g} \rightarrow$	$^3B_{2u}(1b_{1u} \rightarrow 2b_{2g})$	X
		$^3B_{3u}(1b_{1u} \rightarrow 2b_{3g})$	Y
		$^3B_{3u}(1a_u \rightarrow 2b_{2g})$	Y
		$^3B_{2u}(1a_u \rightarrow 2b_{3g})$	X
		$^3A_u(1a_u \rightarrow 1b_{1g})$	Z

In this article, we report the rR spectra of the above-mentioned complexes with excitation into the IVCT and LMCT bands. The enhancement pattern of the vibrational modes will provide experimental evidence for our previous assignments of these bands as $1b_{1u} \rightarrow 2b_{2g}$ and $1a_u \rightarrow 1b_{1g}$ transitions, respectively.

3.2. UV−Vis, Resonance Raman, and IR Spectra. Qualitative Features of rR Spectra. The spectra of the unsubstituted $[Ni^{II}(L)(L^{\bullet})]^{1-}$ complex are shown in Figures 2 and 3. The ~77 K frozen solution rR spectra were obtained for excitations at 840 and 407 nm, which fall into the region of IVCT and LMCT charge-transfer bands, respectively. Upon IVCT excitation, a rich set of vibrational peaks is observed between 150 and 2000 cm^{-1}, which will later be assigned to vibrational fundamentals, overtones, and combination bands. In addition to low-frequency M−S stretching modes, significant enhancement of C−C stretching vibrations (1000−1600 cm^{-1}) indicates significant ligand involvement in the electronic excitation. A similar situation has been found in the case of LLCT bands of two metal diimine−dithiolate complexes.[10] In these systems, several rR fundamentals were identified. These fundamentals correspond to metal−ligand stretching vibrations and to modes localized on either ligands.[10] The rR spectrum for LMCT excitation of the $[Ni^{II}(L)(L^{\bullet})]^{1-}$ complex is dominated by moderately enhanced low-frequency bands (150−700 cm^{-1}) (Figure 3). At 407-nm excitation, the Raman line at ~167 cm^{-1} showed the largest enhancement of all modes. By contrast, the IVCT band is mainly in resonance with intense rR bands at ~360 cm^{-1} and ~1100 cm^{-1}. The latter band shows very little enhancement upon laser excitation into the LMCT band. The large relative enhancement of low-frequency M−S modes has also been found for LMCT bands of oxo-metallo−bis(dithiolenes) and metallo−mono(dithiolene) complexes which was explained by large M−S bond distortions anticipated for bonding−antibonding electronic transitions.[41,42] These characteristic features of rR patterns for both types of electronic transitions are preserved in the case of the butyl-substituted $[Ni^{II}(L^{Bu})(L^{Bu\bullet})]^{1-}$ (Figures S1 and S2) and $[Pt^{II}(L^{Bu})(L^{Bu\bullet})]^{1-}$ compounds (Figure S3).[43] Figure S4 presents the rR spectrum of $[Cu^{III}(L^{Bu})_2]^{1-}$ upon 407-nm excitation. The enhancement pattern is similar to that observed for $[Ni^{II}(L^{Bu})(L^{Bu\bullet})]^{1-}$ and is dominated by intense low-

(41) Inscore, F. E.; McNaughton, R.; Westcott, B. L.; Helton, M. E.; Jones, R. M.; Dhawan, I. K.; Enemark, J. H.; Kirk, M. L. *Inorg. Chem.* **1999**, *38*, 1401.
(42) McNaughton, R. L.; Helton, M. E.; Rubie, N. D.; Kirk, M. L. *Inorg. Chem.* **2000**, *39*, 4386.

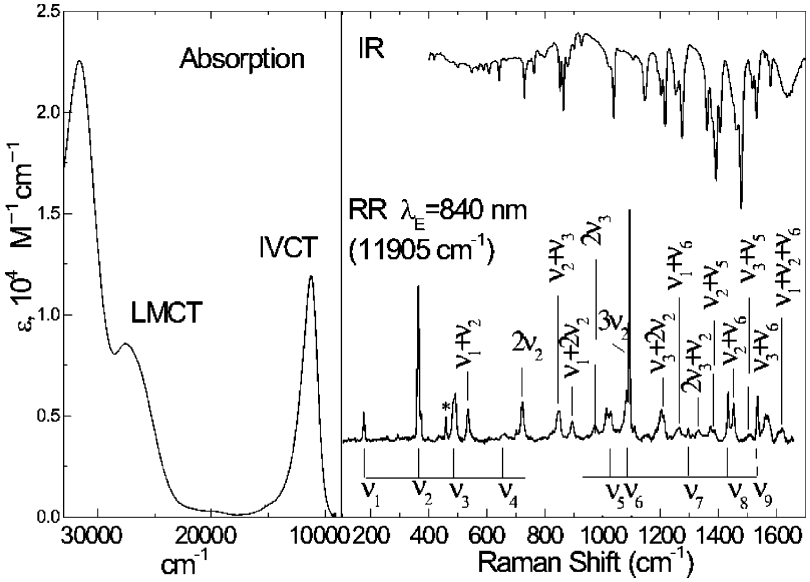

Figure 2. Experimental absorption, IR, and rR spectra (840-nm laser excitation, concentration 5.4×10^{-3} M) of $[Ni^{II}(L)(L^{\bullet})]^{-1}$. See section 2.2 for details. Artifacts and solvent lines are marked with asterisks.

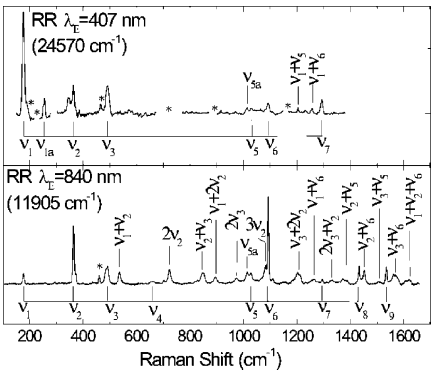

Figure 3. Comparison of rR spectra of $[Ni^{II}(L)(L^{\bullet})]^{-1}$ complex upon 407- and 840-nm laser excitation (concentration 5.4×10^{-3} M). See section 2.2 for details. Artifacts, solvent lines, and spectral regions with removed solvent lines are marked with asterisks.

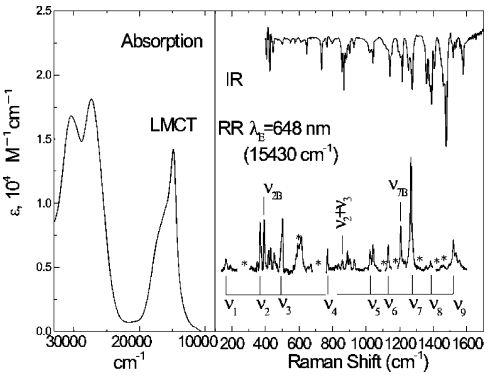

Figure 4. Experimental absorption, IR, and rR spectra (648-nm laser excitation, concentration 3.21×10^{-4} M) of $[Co^{III}(L^{Bu})_2]^{1-}$ complex. See section 2.2 for details. Artifacts, solvent lines, and spectral regions with removed solvent lines are marked with asterisks.

frequency bands. This fact corroborates the assignment of the UV absorption bands for these species, occurring in the range 350−450 nm as LMCT bands.[7d]

The rR spectrum of $[Co^{III}(L^{Bu})_2]^{1-}$ with 648-nm excitation is presented in Figure 4. The assignment of the absorption and MCD spectra for this compound in ref 8 suggests that this region consists of mainly two LMCT transitions that occur at ∼595 nm (16 800 cm^{-1}) and ∼629 nm (15 900 cm^{-1}), respectively. The distinctive feature of the rR spectrum for the $[Co^{III}(L^{Bu})_2]^{1-}$ species is the presence of a very intense Raman band at 1268 cm^{-1}.

Qualitative Features of IR Spectra. A summary of the infrared spectra for solid $[M(L)_2]^z$ and $[M(L^{Bu})_2]^z$ (KBr disks) is displayed in Figure 5. For complexes containing the L^{Bu} ligand, the intense infrared stretch at ∼1100 cm^{-1} has previously been assigned to a C−S stretching vibration and has been taken as indicative for the presence of coordinated dithiobenzosemiquinonate(1−) radicals.[7d] Thus, this band is present in the $[Ni^{II}(L^{Bu})(L^{Bu\bullet})]^{1-}$, $[Pd^{II}(L^{Bu})(L^{Bu\bullet})]^{1-}$, $[Pt^{II}(L^{Bu})(L^{Bu\bullet})]^{1-}$, and $[Au^{III}(L^{Bu})(L^{Bu\bullet})]^{0}$ complexes and is absent in the corresponding $[Cu^{III}(L^{Bu})_2]^{1-}$, $[Co^{III}(L^{Bu})_2]^{1-}$, and $[Au^{III}(L^{Bu})_2]^{1-}$ complexes. An opposite trend, however, is observed for the corresponding complexes involving the unsubstituted L ligand. Here the complexes containing radical ligands lack the infrared stretch at ∼1100 cm^{-1} but this feature is present in the IR spectra of the nonradical complexes.

3.3. Vibrational Assignments. For the molecular orbital and normal-mode description of the complexes within D_{2h} and C_{2h} point groups, we chose the *z*-axis to be perpendicular to the symmetry plane σ_h, the *x*-axis to be along the long axis of the complex, and the *y*-axis to be along the short axis (Figure 1).

General Features. Altogether, the D_{2h} symmetry of the $[M^{II}(L)(L^{\bullet})]^{1-}$ compounds leads to 47 in-plane (12 A_g, 12 B_{3u}, 12 B_{2u}, 11 B_{1g}) and 22 out-of-plane (5 B_{3g}, 5 B_{2g}, 6 B_{1u}, 6 A_u) modes. The calculated frequencies of in-plane vibrations, excluding C−H stretching modes, and their correlation throughout the compounds are documented in the Supporting Information (Table S1).

In the case of $[M^{II}(L^{Bu})(L^{Bu\bullet})]^{1-}$ compounds (C_{2h} symmetry), there are 123 in-plane (61 A_g, 62 B_u) and 90 out-of-plane (44

(43) For the $[Pt^{II}(L^{Bu})(L^{Bu\bullet})]^{1-}$ compound, we have not found clearly resolved resonance Raman bands for the available UV excitations. The 407-nm excitation frequency is too far away from the resonance at 361 nm for this compound (Figure S3), and only a faint peak around 167 cm^{-1} has been found upon 350-nm excitation. The primary reasons for such a discrepancy may be low laser power and possibly a significant role of self-absorption near the resonance that diminishes the resonance Raman scattering intensity.

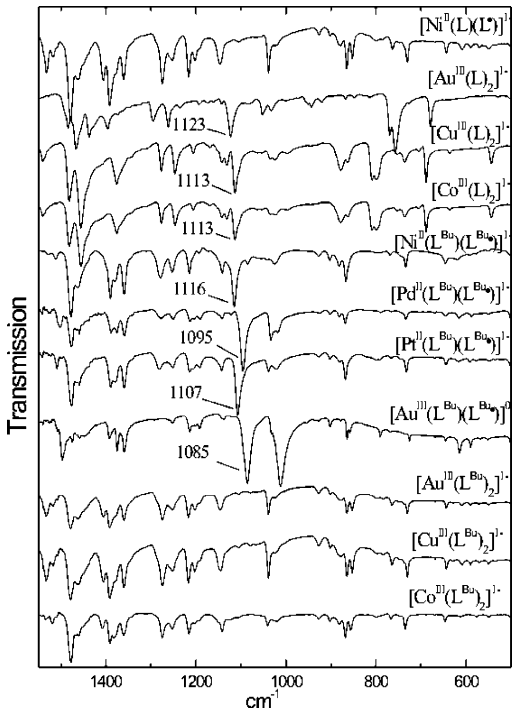

Figure 5. IR spectra of solid $[N(n\text{-}Bu)_4]^+$ salts of $[Ni^{II}(L)(L^{\bullet})]^{-1}$, $[Au^{III}(L)_2]^{1-}$, $[Cu^{III}(L)_2]^{1-}$, $[Co^{III}(L)_2]^{1-}$, $[Ni^{II}(L^{Bu})(L^{Bu\bullet})]^{1-}$, $[Pd^{II}(L^{Bu})(L^{Bu\bullet})]^{1-}$, $[Pt^{II}(L^{Bu})(L^{Bu\bullet})]^{1-}$, $[Au^{III}(L^{Bu})_2]^{1-}$, $[Cu^{III}(L^{Bu})_2]^{1-}$, $[Co^{III}(L^{Bu})_2]^{1-}$, and neutral $[Au^{III}(L^{Bu})(L^{Bu\bullet})]^0$ in the range 500−1500 cm^{-1} (KBr disks).

B_g, 46 A_u) vibrations. Note that both the *tert*-butyl substituted and the unsubstituted complexes are centrosymmetric molecules. Thus, the infrared active fundamentals are Raman inactive and vice versa. The total number of IR active fundamental bands is 30 (12 B_{3u}, 12 B_{2u}, 6 B_{1u}) for the $[M^{II}(L)(L^{\bullet})]^{1-}$ compounds and 108 (62 B_u, 46 A_u) for the $[M^{II}(L^{Bu})(L^{Bu\bullet})]^{1-}$ compounds. Consequently, the *tert*-butyl substituted complexes are expected and observed to reveal richer and more complicated IR spectra compared to that of their more symmetric unsubstituted counterparts (Figure 5). In particular, for compounds containing L^{Bu} instead of L ligands, the number of vibrations involving the ligand and metal ions increases because of their possibility to mix with different types of substituent vibrations. Taking into account that B_{1g} modes (in D_{2h} symmetry) correlate with A_g modes (in C_{2h} symmetry), the number of totally symmetric vibrations for the *tert*-butyl substituted complexes is necessarily larger than that for the unsubstituted ligand. Therefore, the rR spectra of substituted compounds show an increased number of fundamental bands ($0 \rightarrow 1$ transitions) as compared to the spectra of the unsubstituted counterparts (Figures 2 and S1).

Key Vibrational Modes. In analyzing the vibrational modes of the square-planar bis-dithiolenes, we have focused on three main aspects: (a) metal−ligand stretching vibrations, (b) carbon−sulfur stretching vibrations, and (c) C−C ring vibrations, in particular those modes that describe a quinoidal distortion of the rings. The C−C vibrations can conveniently be referenced to the well-known vibrational modes of the benzene molecule (ref 44, Figure S5). These vibrational regions contain information about metal−ligand bonding. The radical character of the sulfur ligands mainly influences the C−S bonds and, to a lesser degree, the conjugation in the ring system.

Since there are four equivalent metal−sulfur and carbon−sulfur bonds, we have four symmetry-adapted vibrational modes associated with their stretching. Corresponding linear combinations and symmetries are summarized in Table S2. A pictorial description of the most important vibrational modes is given in Figure S5.

rR Assignments. Fundamentals. Since all electronic transitions under study are strongly dipole allowed, the Franck−Condon mechanism is expected to dominate the rR enhancement mechanism. Thus, totally symmetric modes dominate the rR spectra and reflect the geometry change upon excitation. Consequently, the dominant features of the rR spectra were assigned to totally symmetric modes.[20,32,45] Quite similar normal-mode compositions were found for the subspace of totally symmetric vibrations of the substituted complexes which, for the most part, also undergo noticeable rR enhancement. Thus, we have used a common numbering ($\nu_1-\nu_9$) for the A_g normal-mode species in the *tert*-butyl substituted and the unsubstituted compounds. The detailed assignments follow from the comparison of calculated and observed vibrational fundamental frequencies, which are presented in Table 2. Some of the A_g vibrations can be viewed as symmetric combinations of ligand-based vibrations that are closely related to benzene modes. The nine most important, totally symmetric, modes for unsubstituted species of D_{2h} symmetry, together with their benzene counterparts, are shown in Figure S5. Another three totally symmetric vibrations for the unsubstituted compounds that are related to C−H deformation and stretching modes appeared to have negligible intensity in the rR spectra. They have not been analyzed further.

rR Assignments. Overtones and Combination Bands. In addition to the totally symmetric fundamentals, the rR spectra also reveal pronounced overtone and combination progressions, as indicated in the assignments given in Figures 2−4. In the assignment of such bands, we have used the fact that, under the approximation of separable harmonic surfaces, their intensities necessarily correlate with those of the fundamental bands.[32,45] The observation of the overtone and combination bands imply noticeable values of the excited-state distortions that will be evaluated in the fitting procedure based on the Heller analysis described in section 4.

Normal-Mode Compositions. According to the calculated values of P_{MS} (Table S1), and in agreement with accepted assignments of related compounds,[9] the metal−sulfur stretches are primarily distributed in the region 140−500 cm^{-1} with a maximum around 350 cm^{-1}. The partitioning function for the C−S stretches, P_{CS}, spans a broader range with maxima at ∼700, ∼1000−1100, and ∼1300 cm^{-1}, respectively. In-plane and out-of-plane carbon ring deformation vibrations fall between 400 and 800 cm^{-1}. As in the case of the benzene molecule, carbon−carbon stretches lie in the range 1000−1500 cm^{-1}.

3.4. The IR "Marker" Band around 1100 cm^{-1}. In ref 7d, it was suggested that the IR band around 1100 cm^{-1} can serve as a marker for the dithiobenzosemiquinonate(1−) radical ions in the $[M(L^{Bu})_2]^z$ species. From our vibrational assignment, this

(44) Wilson, E. B., Jr.; Decius, J. C.; Cross, P. C. *Molecular Vibrations. The Theory of Infrared and Raman Vibrational Spectra*; Dover Publications: New York, 1980.

(45) Myers, A. B.; Mathies, R. A. Resonance Raman Intensities: A Probe of Excited-State Structure and Dynamica. In *Biological Applications of Raman Spectroscopy*; Spiro, T. G., Ed.; Wiley: New York, 1987; Vol. 2, pp 1−58.

Table 2. Calculated (BP86/TZVP) and Experimental Frequencies of the Most Important Totally Symmetric Vibrations that Appear in the rR Spectra of Compounds $[Ni(L)_2]^{1-}$, $[Ni(L^{Bu})_2]^{1-}$, $Pt(L^{Bu})_2]^{1-}$, $[Co(L^{Bu})_2]^{1-}$, and $[Cu(L^{Bu})_2]^{1-}$ and Their Correlation between Unsubstituted and the *tert*-Butyl Substituted Species

	$[Ni(L)_2]^{1-}$		$[Ni(L^{Bu})_2]^{1-}$		$Pt(L^{Bu})_2]^{1-}$		$[Co(L^{Bu})_2]^{1-}$		$[Cu(L^{Bu})_2]^{1-}$	
vibration	calcd	exptl RR	calcd	exptl RR	calcd	exptl RR	calcd	exptl RR	calcd	exptl RR
metal−ligand stretching[46] ν_1	158.4	176	152.3	167	153.3	167	152.5	164	148.4	167
M−S stretching, C−S deformation ν_2	343.7	364	362.7	372	397.9	427	360	369	351	368
ring deformation, C−S stretching ν_3	477.2	492	491	505	493.5	509	490.1	501	488.6	503
ring deformation, C−S stretching ν_4	663.4	662	755.5	—[a]	754.7	—[a]	754.7	771[a]	753.4	—[a]
C−C stretching, C−S stretching ν_5	1016.3	1028	1009.2	—[a]	1009.2	—[a]	1009.2	1022	1009.0	—[a]
C−C stretching, C−S stretching ν_6	1079.2	1093	1111.6	1125	1106.7	1122	1108.7	1132	1124.8	—[a]
C−C stretching ν_7	1324	1296	1306.2	1289	1304.0	1289	1304.4	1268	1302.8	1279
C−C stretching ν_8	1421.1	1433	1383.2	1397	1383.8	1395	1370.8	1384	1390.8	—[a]
C−C stretching ν_9	1522.3	1535	1508.1	1516	1508.4	1516	1508.1	1520	1519.8	1529

[a] Not unambiguously resolved or not detected due to the close proximity of intense solvent lines.

Table 3. Calculated (BP86/TZVP) and Experimental Frequencies of the ν_{6A} Mode for $[M(L)_2]^z$ and $[M(L^{Bu})_2]^z$ Compounds and Corresponding Calculated IR Intensities

	frequency (cm^{-1})		
complex	calcd	exptl	calcd IR intensity (KM/mol)
$[Ni^{II}(L)(L^{\bullet})]^{1-}$	1071.9	n.d.[a]	7.1
$[Ni^{II}(L^{Bu})(L^{Bu\bullet})]^{1-}$	1105.4	1116	49.1
$[Pd^{II}(L)(L^{\bullet})]^{1-}$	1062.3	—[b]	2.9
$[Pd^{II}(L^{Bu})(L^{Bu\bullet})]^{1-}$	1096.1	1095	143.1
$[Pt^{II}(L)(L^{\bullet})]^{1-}$	1064.6	—[b]	0.2
$[Pt^{II}(L^{Bu})(L^{Bu\bullet})]^{1-}$	1098.9	1107	85.6
$[Cu^{III}(L)_2]^{1-}$	1093.9	1113	242.9
$[Cu^{III}(L^{Bu})_2]^{1-}$	1124.4	n.d.[a]	34.1
$[Au^{III}(L)_2]^{1-}$	1087.5	1123	210.4
$[Au^{III}(L^{Bu})_2]^{1-}$	1118.0	n.d.[a]	27.5
$[Au^{III}(L^{Bu})(L^{Bu\bullet})]^{0}$	1091.3	1085	479.3
$[Co(L)_2]^{1-}$	1077.1	1113	108.4
$[Co(L^{Bu})_2]^{1-}$	1104.4	n.d.[a]	42.9

[a] n.d. = not detected. [b] Experimental data are not available.

band corresponds to a B_{3u} symmetry vibration (ν_{6a}; Figure S5), involving C−C and C−S bond stretching. It is a nontotally symmetric counterpart of the ν_6 mode observed in the rR experiments. Indeed, upon inspection of the IR spectra in Figure 5, we found that ν_{6a} correlates well with our assignment of a radical species along the series of complexes.

However, according to the IR spectra (Figure 5) and results of DFT calculations (Table 3) for the $[M(L^{Bu})_2]^z$ and $[M(L)_2]^z$ species, it was found that the IR intensity of the ν_{6a} mode shows dramatic dependence on the substitution pattern of the benzene ring. Thus, the unsubstituted, nonradical complexes $[M^{III}(L)_2]^{1-}$ (Cu, Co, Au) reveal a strong enhancement of the ν_{6a} mode, whereas in the radical-like species $[Ni^{II}(L)(L^{\bullet})]^{-1}$ this is not observed. For the corresponding *tert*-butyl substituted complexes, this behavior is reversed. For the $[M^{III}(L^{Bu})_2]^{1-}$ (M = Au, Cu, Co) species the ν_{6a} mode at ~1100 cm^{-1} is not observed, whereas in the radical species $[M^{II}(L^{Bu})(L^{Bu\bullet})]^{1-}$ (M = Ni, Pd, Pt) and $[Au^{III}(L^{Bu})(L^{Bu\bullet})]^0$ this mode is clearly present with appreciable intensity. Clearly, it cannot be ruled out that, for other substitution patterns, the IR intensity of the ν_{6a} mode could show even more complicated behavior. Thus, the IR band around ~1100 cm^{-1} is not an exceedingly reliable marker for the presence of sulfur-based radicals. As will be evident below, the rR intensities are preferred for this purpose. The underlying reason is that the rR intensities of the ligand-based normal modes that are coupled to a given electronic transition do not change significantly upon their possible mixture with various substituent vibrations. By contrast, the relative IR intensities strongly depend on the nature of substituents, since the latter are characterized by a certain electric charge distribution. This can make large uncompensated contributions to the total vibrationally induced electric dipole moment that ultimately may severely affect the corresponding IR intensity.

3.5. Direct Quantum Chemical Calculation and Time-Dependent Analysis of rR Spectra. In section 3.2, it was observed that the enhancement pattern for an LMCT band differs dramatically from that of an IVCT band, which allows the deduction of the type of electronic transition from the rR enhancement pattern. To obtain more insight into these enhancement patterns, electronic structure calculations were performed to estimate the excited-state dimensionless normal coordinate displacements (Δ_i^I where i labels normal modes, and I electronic states).[47] Having obtained reasonable estimates of the nonzero Δ_i^I, theoretical rR spectra can be deduced by combining these displacements with transition energies, transition moments, as well as a phenomenological line width parameter obtained from fitting the absorption band shape. Since the theoretical displacements turned out to be reasonably accurate, they needed little refinement in the subsequent fitting of the rR intensities. Note that it is sufficient to fit a single rR spectrum together with the absorption band shape to obtain the displacements of all modes that are in resonance with the electronic transition studied.[48]

The calculations were performed at two different levels of theory, namely TD-DFT and MR-DDCI2. The latter is a genuine, albeit simplified, multireference ab initio method and is expected to be more balanced than TD-DFT in the description of excited states. The calculated vertical transition energies from the two methods are compared to the experimental estimates in Table 4 and show good agreement with experiment which corroborates the assignment of the absorption spectra. The

(46) Although the ν_1 and ν_2 modes have predominantly M−S stretching character, there is a subtle difference between the shapes of these two vibrations. The first mode involves a translational motion of the two ligands in opposite directions with no deformation or bond stretching except for the M−S bonds. For the ν_2 mode the M−S stretching is accompanied by a considerable in-plane deformation of the MS_2C_2 pentagon while the aromatic rings remain fixed. Therefore, we have denoted ν_1 as "metal−ligand stretching" and ν_2 as ("M−S stretching, C−S deformation").

(47) Normal modes are only defined up to an arbitrary choice of sign. Consequently, the absolute sign of Δ_i^I is ambiguous, whereas the relative signs of Δ_i for different I are of course meaningful. This has only consequences for the shape of the rR spectra and excitation profiles if the transitions studied have nonperpendicular polarizations. In the present work, Δ_i^I are calculated and fitted for transitions with different polarizations. Therefore, neither the absorption band shape nor the rR intensities depend on the signs of the Δ_i^I. For convenience, we present only the absolute values of the dimensionless normal coordinate displacements.

(48) Myers, A. B.; Mathies, R. A.; Tannor, D. J.; Heller, E. J. *J. Chem. Phys.* **1982**, *77*, 3857.

Table 4. Comparison of Calculated Vertical Transition Energy with Experimentally Determined Band Maxima (in cm^{-1}) for the Range of Complexes and Electronic States Studied by rR Spectroscopy in This Work

complex	excited state	TD-DFT	MR-DDCI2	exptl
$[Ni^{II}(L)(L^{\bullet})]^{1-}$	$^2B_{1u}(1b_{1u} \rightarrow 2b_{2g})$	13 462	12 752	11 407
	$^2A_u(1a_u \rightarrow 2b_{2g})$	12 810	14 585	11 763
	$A\text{-}^2B_{3u}(1a_u \rightarrow 1b_{1g})$	19 478	25 652	26 155
	$B\text{-}^2B_{3u}(1a_u \rightarrow 1b_{1g})$	21 067	30 770	—[a]
$[Cu^{III}(L)_2]^{1-}$	$1B_{1u}(1au \rightarrow 1b_{1g})$	11 600	15 715	24 616
$[Co(L)_2]^{1-}$	$^3B_{2u}(1b_{1u} \rightarrow 2b_{2g})$	16 465	15 566	15 640
	$^3B_{3u}(1a_u \rightarrow 2b_{2g})$	15 632	16 275	15 160

[a] Not observed.

exception is the $[Cu^{III}(L)_2]^{1-}$ complex, for which the error in the calculated transition energy exceeds 10 000 cm^{-1}. We have observed similar failures for other mononuclear copper complexes as well. In these cases, more elaborate multireference approaches, with much larger basis sets, are necessary to achieve accurate results, and these are computationally too demanding to apply them to the calculation of rR intensities in this work. The results below nevertheless indicate that despite the large error in the transition energy, the calculated excited-state potential energy surface must be reasonably parallel to the real one, since the rR intensities are still well predicted by the calculations. We also note that the incapability of TD-DFT to correctly describe the two $^2B_{3u}$ excited states, in the case of $[Ni^{II}(L)(L^{\bullet})]^{1-}$, precludes the application of this method to the prediction of rR intensities for these two states. However, the MR-DDCI2 method does not have any problems with the two alternative spin couplings (vide supra). Further evidence for the correct assignment of the electronic states will come from the detailed consideration of the rR intensities in the following sections.

In addition to detailed calculations, we will outline below a simple qualitative method that, in many cases, can explain the observed enhancement patterns without the need to perform elaborate quantum chemical calculations. All that is needed are the shapes of the normal modes involved and an electronic difference density from some kind of excited-state calculation that we take to be TD-DFT together with the BP86 functional in the present case since this maintains the consistency with the ground-state geometry optimization and frequency calculations.

3.5.1. $[Ni^{II}(L)(L^{\bullet})]^{1-}$. $1b_{1u} \rightarrow 2b_{2g}$ and $1a_u \rightarrow 2b_{2g}$ IVCT Transitions. The intense absorption feature in the NIR, shown in Figure 2, can be decomposed into two bands that are assigned to $1b_{1u} \rightarrow 2b_{2g}$ and $1a_u \rightarrow 2b_{2g}$ IVCT transitions.[7d] The observed rR spectra (Figure 2) are obtained using laser excitation at 11 900 cm^{-1}, which falls in the region of both the above transitions. Thus, both of them make significant contribution to the rR pattern and need to be accounted for in the fitting procedure.

The observed spectra are dominated by an intense ν_2 at ~350 cm^{-1} and a ν_6 band at ~1100 cm^{-1}. The calculated and fitted dimensionless normal coordinate displacements are compared in Table 5. However, despite large values found for Δ_1, mode ν_1 has a rather small rR intensity. This is explained by the significant frequency dependence of the rR intensities and more narrow excitation profiles for low-frequency modes as compared to high-frequency ones.

Enhancement Mechanism for $1b_{1u} \rightarrow 2b_{2g}$ Transitions. For this type of transition, the donor $1b_{1u}$ MO is the bonding combination of the HOMO ($2b_2$) of two L^{2-} ligands,[7d] while the acceptor $2b_{2g}$ level is the antibonding combination. The b_{2g} ligand fragment π-MO can undergo a symmetry-allowed back-bonding interaction with the Ni d_{xz} orbital and was analyzed in detail previously.[7d] Accordingly, the difference density plot for a $1b_{1u} \rightarrow 2b_{2g}$ transition (Figure 6) indicates a loss of bonding for the M−S, C_3-C_4, C_1-C_2, C_1-C_6, and C_5-C_6 bonds, thus leading to their lengthening in the electronically excited state. At the same time, the C−S bonds are expected to contract.

Consequently, in addition to the expected M−S bond elongation, the geometry changes associated with the $1b_{1u} \rightarrow 2b_{2g}$ excitation have a significant component that corresponds to quinoidal distortion (elongation of C_1-C_2, C_1-C_6, and C_5-C_6 bonds) of the aromatic ring. The totally symmetric normal modes with the largest projections onto this elongation and contraction pattern are expected to show the dominant enhancement in the rR spectra. These criteria are met by the ν_1 (~170 cm^{-1}), ν_2 (~350 cm^{-1}), and ν_6 (~1100 cm^{-1}) modes (Figure 6). The latter mode features in-phase stretching of C_1-C_2, C_1-C_6, and C_5-C_6 bonds, and thus has the largest projection onto the quinoidal component of the excited-state distortion among the other C−C stretching vibrations.

Enhancement Mechanism for $1a_u \rightarrow 2b_{2g}$ Transitions. For a $1a_u \rightarrow 2b_{2g}$ IVCT transition, the main difference is that the donor $1a_u$ MO is a nonbonding combination of the $2a_2$ MOs of two L^{2-} fragment orbitals.[7d] This implies less elongation of the M−S bonds upon excitation as compared to the $1b_{1u} \rightarrow 2b_{2g}$ case and explains why the calculated excited-state displacements Δ_1 and Δ_2 along M−S modes have smaller values (Table 5). The difference density plot for a $1a_u \rightarrow 2b_{2g}$ transition (Figure 7) indicates a loss of bonding for the C_2-C_3 and C_4-C_5 bonds and gain of bonding forces for the C_1-C_6 bond, thus leading to the lengthening of the former and contraction of the latter in the excited state. Similar to the case of a $1b_{1u} \rightarrow 2b_{2g}$ transition, such a distortion pattern has a significant projection onto the ν_6 mode. In addition, there are significant projections of the excited-state distortion onto the ν_7 and ν_8 modes, both of which feature in-phase stretching of C_2-C_3 and C_4-C_5 bonds. The net effect is that, according to the calculations and the fit to the experimental data, the excited-state displacements along ν_6, ν_7, and ν_8 are almost equal upon $1a_u \rightarrow 2b_{2g}$ excitation (Table 5).

Simulated Resonance Raman and Electronic Absorption Spectra. The simulated rR spectra, based on the $\{\Delta_i^I\}$ obtained from the fit and MR-DDCI2 calculations, are found to be in reasonable agreement with experiment (Figure 8), whereas the rR pattern predicted by TD-DFT calculations reveals only qualitative agreement. The fit between 9000 and 17 000 cm^{-1} clearly indicates that the peculiar band shape of the intense near-IR IVCT transition results from the superposition of two electronic band systems, consistent with the previous assignment.[7d] Together with the significant vibronic broadening, the effective bandwidth is almost 2.5 times higher than the homogeneous line width.

3.5.2. $[Co(L)_2]^{1-}$. $1b_{1u} \rightarrow 2b_{2g}$ and $1a_u \rightarrow 2b_{2g}$ LMCT Transitions. As analyzed in detail previously, $[Co(L)_2]^{1-}$ has a much higher metal character (65% $3d_{xz}$) in the acceptor $2b_{2g}$ MO as compared to that in $[Ni^{II}(L)(L^{\bullet})]^{1-}$ (34% $3d_{xz}$).[8] The enhanced metal character suggests that the loss of bonding

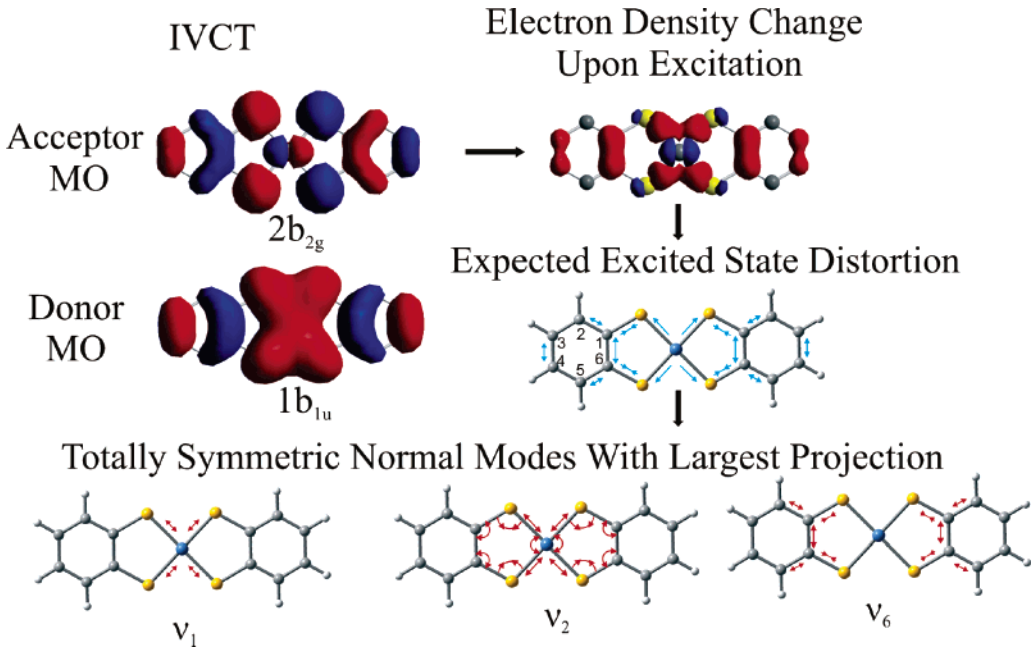

Figure 6. Normal modes with the largest excited-state displacements for the IVCT $1b_{1u} \rightarrow 2b_{2g}$ transition of $[Ni^{II}(L)(L^{\bullet})]^{1-}$ and their relation to the nature of excitation. Donor and acceptor MOs were obtained from spin-unrestricted BP86 DFT calculations. The corresponding electronic difference density is plotted for the isodensity value of 0.0008 au (red and blue colors indicate a decrease and increase of the electronic density in the excited state, respectively). Bond length changes upon excitation are represented by outward arrows (bond elongation) and inward arrows (bond contraction). In the normal-mode representation, the length of arrows and arch lines roughly designates the relative amplitude of bond stretching and bending, respectively. Internal coordinates vibrating in antiphase are denoted by inward and outward arrows.

Table 5. Fitted {for $[Ni^{II}(L)(L^{\bullet})]^{1-}$ and $[Co(L^{Bu})_2]^{1-}$} and Calculated {for $[Ni^{II}(L)(L^{\bullet})]^{1-}$ and $[Co(L)_2]^{1-}$} Dimensionless Normal Coordinate Displacements for $1b_{1u} \rightarrow 2b_{2g}$ and $1a_u \rightarrow 2b_{2g}$ Electronic Transitions Obtained from the MR-DDCI2 and Spin-Unrestricted BP86 DFT Methods

	$[Ni(L)_2]^{1-}$						$[Co(L)_2]^{1-}$					
	$1b_{1u} \rightarrow 2b_{2g}$			$1a_u \rightarrow 2b_{2g}$			$1b_{1u} \rightarrow 2b_{2g}$			$1a_u \rightarrow 2b_{2g}$		
	TD-DFT	MR-DDCI2	fit	TD-DFT	MR-DDCI2	fit	TD-DFT	MR-DDCI2	fit[49]	TD-DFT	MR-DDCI2	fit[49] ($[Co(L^{Bu})_2]^{1-}$)
Δ_1	1.74	1.92	1.90	0.83	0.46	0.65	1.79	1.85	1.76	0.88	1.08	1.13
Δ_2	1.03	1.47	1.36	0.50	0.72	0.99	1.36	2.22	$\Delta_2 = 1.41$	0.82	1.35	$\Delta_2 = 0.94$
									$\Delta_{2B} = 1.37$			$\Delta_{2B} = 0.85$
Δ_3	0.51	0.73	0.52	0.36	0.45	0.67	0.6	1.28	1.30	0.2	0.16	0.12
Δ_4	0.03	0.19	0.09	0.12	0.04	0.22	0.05	0.24	0.44	0.1	0.01	0.24
Δ_5	0.08	0.16	0.16	0.0	0.05	0.07	0.1	0.10	0.10	0.04	0.03	0.06
Δ_6	0.18	0.57	0.44	0.26	0.37	0.46	0.24	0.71	0.44	0.13	0.03	0.04
Δ_7	0.07	0.12	0.02	0.35	0.39	0.31	0.03	0.04	$\Delta_7 = 0.01$	0.32	0.55	$\Delta_7 = 0.59$
									$\Delta_{7B} = 0.03$			$\Delta_{7B} = 0.35$
Δ_8	0.08	0.31	0.20	0.31	0.35	0.32	0.13	0.47	0.29	0.21	0.14	0.04
Δ_9	0.09	0.20	0.19	0.22	0.17	0.19	0.10	0.23	0.29	0.15	0.04	0.00

between the metal and the ligand is even more pronounced and leads to larger values of the displacements of the predominantly M−S stretching based Δ_1 and Δ_2. This expectation is confirmed by the experimental and theoretical values collected in Table 5. The exception is the value of Δ_1, which corresponds to the $1b_{1u} \rightarrow 2b_{2g}$ transition and was found to be the same for both compounds. The difference density plot for a $1b_{1u} \rightarrow 2b_{2g}$ transition of $[Co(L)_2]^{1-}$ (Figure S6) reveals that, in the carbon ring, the most significant loss of bonding occurs for the C_1-C_6 bond, thus leading to its elongation. As for the case of the $1b_{1u} \rightarrow 2b_{2g}$ IVCT band of $[Ni(L)_2]^{1-}$, the described geometry changes have the largest projection onto the ν_6 mode.

The difference density plot for the $1a_u \rightarrow 2b_{2g}$ transition of $[Co(L)_2]^{1-}$ shows a loss of bonding for the C_2-C_3 and C_4-C_5 bonds, thus resulting in their elongation. This pattern of quinoidal distortion has the largest projection onto ν_7 mode, which features in-phase stretching of the C_2-C_3 and C_4-C_5 bonds (Figure 9).

In ref 8, the room-temperature absorption and low-temperature MCD spectra of $[Co(L^{Bu})_2]^{1-}$ have been subjected to Gaussian deconvolution in the range 22 000−10 000 cm^{-1}. This yielded a total of seven detectable transitions below 22 000 cm^{-1}. The positions of the most intense $1b_{1u} \rightarrow 2b_{2g}$ and $1a_u \rightarrow 2b_{2g}$ LMCT transitions were found to be at 14 890 and 15 900 cm^{-1}, respectively. According to the distortion pattern outlined above, the rR spectrum of the $1b_{1u} \rightarrow 2b_{2g}$ transition should be dominated by the ν_6 (1132 cm^{-1}) mode in the C−C stretching frequency region (1000−1600 cm^{-1}). However, the rR patterns observed for 14 900 and 15 430 cm^{-1} excitations reveal strong enhancement of the ν_7 (1268 cm^{-1}) mode (Figure 4), which is the signature of a $1a_u \rightarrow 2b_{2g}$ LMCT transition. To resolve this discrepancy, one needs to consider the band shapes of the two types of transitions that were not attempted in the previous analysis.

According to the calculations, the magnitudes of the dimensionless displacements Δ_1, Δ_2, and Δ_3 are much larger for the

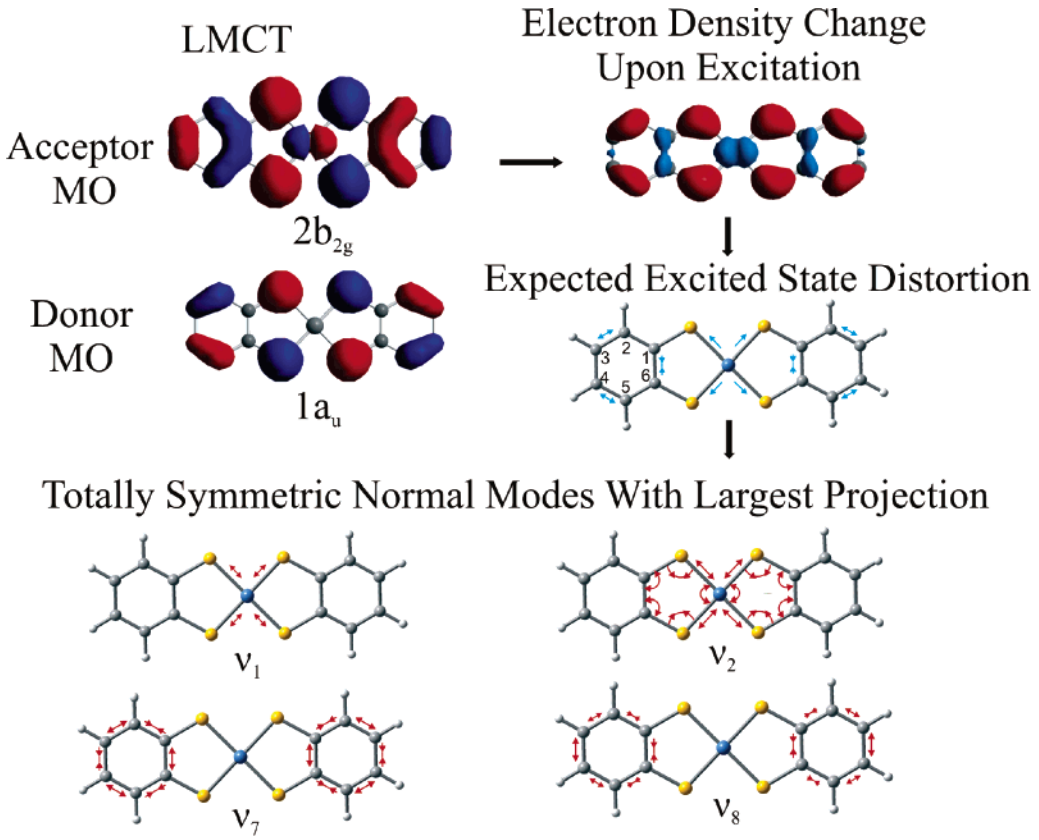

Figure 7. Normal modes with the largest excited-state displacements for the IVCT $1a_u \rightarrow 2b_{2g}$ transition of $[Ni^{II}(L)(L^{\bullet})]^{1-}$ and their relation to the nature of excitation. Donor and acceptor MOs obtained from spin-unrestricted BP86 DFT calculations. The corresponding electronic difference density is plotted for the isodensity value of 0.0008 au (red and blue colors indicate a decrease and increase of the electronic density in the excited state, respectively). Bond length changes upon excitation are schematically represented by outward arrows (bond elongation) and inward arrows (bond contraction). In the normal-mode representation, the length of arrows and arch lines roughly designates the relative amplitude of bond stretching and bending, respectively. Internal coordinates vibrating in antiphase are denoted by inward and outward arrows.

$1b_{1u} \rightarrow 2b_{2g}$ transition compared to that of the $1a_u \rightarrow 2b_{2g}$ (Table 5) transition, which leads to an enhanced vibronic broadening of the corresponding absorption band (and rR profile) by more than a factor of 1.5. As a consequence of the different band shapes, it is also necessary to slightly adjust the position of the band centers. Second, it follows from the time-dependent theory of rR spectroscopy that the presence of the large distortion along low-frequency modes damps their own rR intensities as well as rR intensities of high-frequency C−C stretching vibrations. In the present case, this accounts for a reduction by a factor of ~3 for $1b_{1u} \rightarrow 2b_{2g}$ transition as compared to that of $1a_u \rightarrow 2b_{2g}$ transition.[50] In the final fit of absorption spectrum seven Lorentzian bands were used, consistent with the experimentally observed peaks and shoulders. For simplicity, zero values of excited-state normal-mode displacements were assumed for all transitions, except for the $1b_{1u} \rightarrow 2b_{2g}$ and $1a_u \rightarrow 2b_{2g}$ transitions, which are of predominant interest in this study. In fitting the rR spectra of $[Co(L^{Bu})_2]^{1-}$ (C_{2h} symmetry), only the counterparts of the totally symmetric $\nu_1-\nu_9$ modes of $[Co(L)_2]^{1-}$ were taken into account. Other totally symmetric modes with B_{1g} parentage do not have noticeable rR intensity and thus give negligible contributions to the absorption band shape. The exceptions are the ν_{2B} Co−S (392 cm^{-1}) and ν_{7B} C−C (1207 cm^{-1}) stretching modes with B_{1g} parentage and having noticeable rR intensities (Figure 10). After the joint fit of absorption spectrum and rR intensities, the vertical transition energies for the $1b_{1u} \rightarrow 2b_{2g}$ and $1a_u \rightarrow 2b_{2g}$ transitions are found to be at 15 640 and 15 160 cm^{-1}, respectively (Figure 10); the corresponding adiabatic minima separation energies reveal the reverse order and are equal to 13 890 cm^{-1} (for $1b_{1u} \rightarrow 2b_{2g}$ transition) and 14 520 cm^{-1} (for $1a_u \rightarrow 2b_{2g}$ transition).

3.5.3. $1a_u \rightarrow 1b_{1g}$ LMCT Transition. $[Cu(L)_2]^{1-}$ and $[Ni^{II}(L)(L^{\bullet})]^{1-}$. As analyzed previously, the $[M(L)_2]^z$ and $[M(L)(L^{\bullet})]^z$ species (M = Ni, Pd, Pt, Au, Cu) exhibit an intense *z*-polarized LMCT $1a_u \rightarrow 1b_{1g}$ transition in the UV region <400 nm.[7d] It has been shown in ref 7d that $[M(L)_2]^{1-}$ (M = Ni, Cu) has a metal $3d_{xy}$ character of 46% for $[Ni(L)_2]^{1-}$and of 33% for $[Cu(L)_2]^{1-}$ in the acceptor, $1b_{1g}$, MO. Thus, upon $1a_u \rightarrow 1b_{1g}$ transition, a strongly M−S σ-antibonding orbital is populated in both cases, which leads to a significant elongation of the M−S bonds (Figure 11). Accordingly, the predominantly M−S stretching based Δ_1 and Δ_2 displacements have large values (Table 6), and the rR spectra of these compounds are dominated by low-frequency modes (Figures 12 and S7). The difference density plot for the $1a_u \rightarrow 1b_{1g}$ transition of

(49) Upon symmetry lowering from D_{2h} in the unsubstituted complexes to C_{2h} in the substituted complexes, the excited-state distortions along the ν_2 and ν_7 modes acquire additional strong components along the ν_{2B} and ν_{7B} modes. This is partly due to a mixing of ν_2 (ν_7) with ν_{2B} (ν_{7B}) and partly due to changes in the shapes of the excited-state distortion upon symmetry lowering. Therefore, we have found it to be appropriate to compare $\Delta_N(D_{2h})$ calculated for $[M(L)_2]^z$ complexes with both $\Delta_N(C_{2h})$ and $\Delta_{NB}(C_{2h})$ ($N = 2, 7$) determined in the fitting of the rR data obtained for the $[M(L^{Bu})_2]^z$ species. Because $\nu_2 \approx \nu_{2B}$ and $\nu_7 \approx \nu_{7B}$, one expects the following correlation between the high- and low-symmetry parameters: $(\Delta_N)^2(D_{2h}) \approx (\Delta_N)^2(C_{2h}) + (\Delta_{NB})^2(C_{2h})$.

(50) In these model calculations, both bands had the same positions and transition dipole moments.

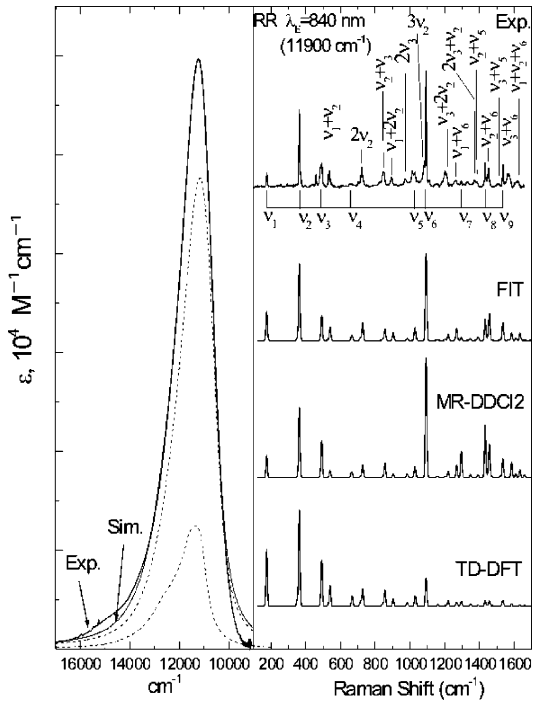

Figure 8. Deconvoluted absorption spectrum of $[Ni^{II}(L)(L^{\bullet})]^{1-}$ in the range 9000−17 000 cm^{-1} (left). The component electronic bands are represented by dashed curves. Experimental and simulated rR spectra (right) corresponding to dimensionless normal coordinate displacements obtained from the fit, MR-DDCI2 and spin-unrestricted BP86 DFT calculations (Table 5).

$[Ni^{II}(L)(L^{\bullet})]^{1-}$ (Figure 11) shows also the loss of bonding in the C_2-C_3 and C_4-C_5 bonds, resulting in their elongation. For the LMCT $1a_u \rightarrow 2b_{2g}$ transition of $[Co(L)_2]^{1-}$, this pattern of quinoidal distortions has the largest projection onto the ν_7 mode, which features in-phase stretching of the C_2-C_3 and C_4-C_5 bonds (Figure 11). Despite the qualitative similarities of the MO pictures for the analogous $1a_u \rightarrow 1b_{1g}$ LMCT transitions, the dimensionless displacements Δ_1 and Δ_2 have rather different relative values for the $[Cu(L)_2]^{1-}$ and $[Ni^{II}(L)(L^{\bullet})]^{1-}$ species. In $[Cu(L)_2]^{1-}$, Δ_1 is rather close to Δ_2; however, for $[Ni^{II}(L)(L^{\bullet})]^{1-}$ Δ_1 is significantly larger than Δ_2 (Table 6). Presumably, this originates from a more pronounced M−S σ-antibonding character for the $1b_{1g}$ acceptor orbital of $[Cu(L)_2]^{1-}$ compared to that of $[Ni^{II}(L)(L^{\bullet})]^{1-}$. This ultimately leads to larger distortions primarily along the ν_2 mode rather than along ν_1. Consequently, the rR spectrum of the $[Ni^{II}(L)(L^{\bullet})]^{1-}$ species is dominated by the ν_1 mode, whereas for $[Cu(L)_2]^{1-}$ the largest enhancement is observed for the ν_2 vibration.

MR-DDCI2 calculations predict values of 25 652 and 30 770 cm^{-1}, respectively, for the vertical transition energies between the ground state and the two components of the $1a_u \rightarrow 1b_{1g}$ ($^2B_{3u}$ state) transitions of $[Ni^{II}(L)(L^{\bullet})]^{1-}$, which correspond to the two alternative spin couplings (eqs 1 and 2). Both excited states have very similar values of the dimensionless normal coordinate displacements. According to our assignment of the experimental spectrum, the lower component corresponds to the experimentally observed transition at ∼26 100 cm^{-1}, and its calculated Δ_i^I values are listed in Table 6.

In the fit, only the red edge of the absorption band, with maximum absorbance around 400 nm, was taken into account since at higher energies other bands, which are not yet assigned, also contribute. In fitting the rR spectra of $[Cu(L^{Bu})_2]^{1-}$ (C_{2h} symmetry), the counterparts of the totally symmetric $\nu_1-\nu_3$ and ν_9 modes of $[Cu(L)_2]^{1-}$, which are clearly identified in the experiment, have been taken into account. Similar to the case of $[Co(L^{Bu})_2]^{1-}$, the intensities of the ν_2 (368 cm^{-1}) and ν_7 (1279 cm^{-1}) modes are partially transferred to the totally symmetric modes of B_{1g} parentage: ν_{2B} (390 cm^{-1}) and ν_{7B} (1204 cm^{-1}) (Figure 12), respectively. Therefore, the latter were also included in the fit (Table 6).

The $\{\Delta_i^I\}$ values obtained from MR-DDCI2 (for $[Ni^{II}(L)(L^{\bullet})]^{1-}$ and $[Cu(L)_2]^{1-}$) and TD-DFT (for $[Cu(L)_2]^{1-}$) calculations are found to be in reasonable agreement with the fitted displacements (Table 6). In this case, MR-DDCI2 method tends to overestimate the Δ_i^I values for C−C stretching modes.[51] Both TD-DFT and MR-DDCI2 calculations somewhat underestimate Δ_1 and overestimate Δ_2 parameters, which, according to the shape of ν_1 and ν_2 modes, implies that both methods overestimate the deformation of the MS_2C_2 pentagon in the excited state.

4. Discussion and Conclusions

Square-planar transition metal dithiolenes in various oxidation states have been found to display very intense electronic transitions in the visible region of the spectrum.[7d,8,11c,21] In this work, we have studied these transitions in a series of prototypical complexes in depth using a combination of resonance Raman spectroscopy and quantum chemistry. These studies have defined the information content of absorption and rR spectroscopy for the compounds investigated. In particular, it was shown that the observed rR enhancement pattern of the molecules under investigation correlates strongly with the nature of the electronic transition. Thus, transitions that preferentially enhance the ν_6 mode at ∼1100 cm^{-1} containing significant C−S stretching character represent IVCT transitions. Since such transitions can only occur when the ligands have significant open-shell character, the observation of such bands is indicative of coordinated ligand-based radicals. This situation sharply contrasts with the situation found for ligand-to-metal charge-transfer transitions, which preferentially enhance the ν_1 and ν_2 modes which are dominated by metal−sulfur stretchings.

These qualitative considerations can be quantified by determining the dimensionless displacement parameters, $\{\Delta_i^I\}$, for each mode, *i*, and each electronic transition, *I*. By using the popular time-dependent theory of Heller and co-workers,[32] which leads to easily manageable expressions even in the presence of many modes and multiple electronic transitions, these displacements were obtained by simultaneously fitting the absorption and rR spectra of the complexes under investigation. Second, these displacements have been calculated by TD-DFT and simplified correlated multireference ab initio methods, which provided very good starting values for the experimental fitting

(51) In the current study, vibronic coupling, B-term sources of rR intensities, and nonadiabatic effects were neglected. However, they can be quite important in the present case due to the high density of states in the UV region, thus affecting the accuracy of the fitted parameters. In addition, it is known that the homogeneous broadening induces interference effects, while inhomogeneous broadening cannot lead to noticeable variations in the rR intensities.[48] The homogeneous line widths obtained from the fit for the $1a_u \rightarrow 1b_{1g}$ band are equal to 750 cm^{-1} (for $[Ni^{II}(L)(L^{\bullet})]^{1-}$) and 1030 cm^{-1} (for $[Cu^{III}(L^{Bu})_2]^{1-}$), which seem to be unphysically large.[48] Such large homogeneous line widths ultimately compensate for neglected inhomogeneous contributions. At the same time, the large Γ-factors artificially damp the intensities of low-frequency modes relative to high-frequency modes. Thus, in the mixed homogeneous−heterogeneous case, better agreement is expected between the fitted and calculated $\{\Delta_i^I\}$.

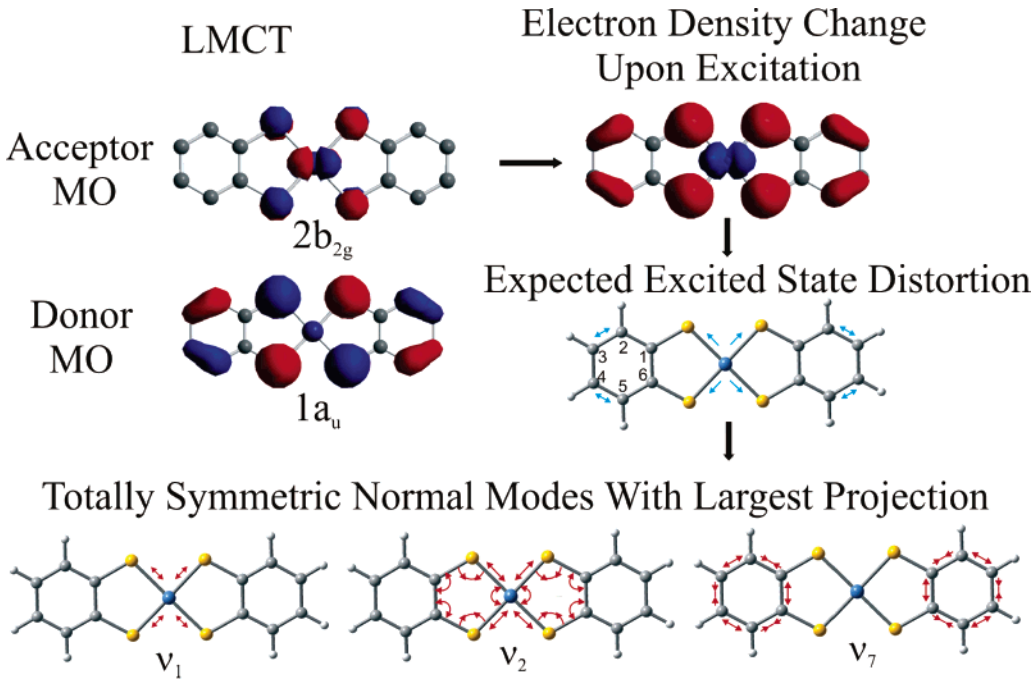

Figure 9. Normal modes with the largest excited-state displacements for the LMCT $1a_u \rightarrow 2b_{2g}$ transition of $[Co(L)_2]^{1-}$ and their relation to the nature of excitation. Donor and acceptor MOs were obtained from spin-unrestricted BP86 DFT calculations. The corresponding electronic difference density is plotted for the isodensity value of 0.0008 au (red and blue colors indicate a decrease and increase of the electronic density in the excited state, respectively). Bond length changes upon excitation are represented by outward arrows (bond elongation) and inward arrows (bond contraction). In the normal-mode representation, the length of arrows and arch lines roughly designates the relative amplitude of bond stretching and bending, respectively. Internal coordinates vibrating in antiphase are denoted by inward and outward arrows.

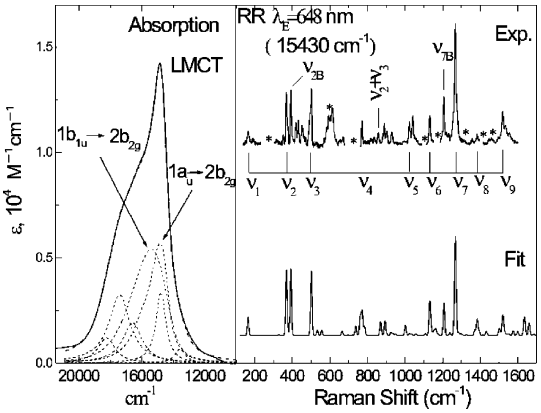

Figure 10. Deconvoluted absorption spectrum of $[Co(L^{Bu})_2]^{1-}$ in the range 10 000−21 000 cm^{-1} (left), and experimental and simulated rR spectra (right) corresponding to dimensionless normal coordinate displacements obtained from the fit (Table 5). Artifacts, solvent lines, and spectral regions with removed solvent lines are marked with asterisks.

procedures. Furthermore, it was also shown that the calculations provide qualitative insight into the nature of the observed excited-state distortions, and a simple graphical procedure was outlined that allows one to estimate the dominantly enhanced modes even from simple excited-state calculations.

In addition, we have studied the IR spectra of the entire series of transition metal dithiolenes. The observation of a strong C−S stretching band (ν_{6a}) at ∼1100 cm^{-1} has previously been used as a marker band for the detection of ligand-based oxidations.[7d,11c] However, in this article, it is experimentally and theoretically shown that the intensity of these IR bands strongly depends on the nature of the substituents in the periphery of the phenyl ring. Thus, the intensity mechanism is indirect and unreliable as a primary electronic marker of radical character. In this respect, rR spectroscopy in the near-IR and visible regions is strongly preferred, since the intensities of the dominantly enhanced modes are virtually independent of substituent effects.

This work also has a significant methodological component with respect to the analysis of rR spectra. rR intensities have been used to determine excited-state distortions for a number of molecules.[10,48,52−56] In particular, excited-state distortions resulting from CT excited states of inorganic and organic molecules have been of special interest.[10,53,56] On the other hand, only a few studies have been devoted to theoretical prediction of rR spectra using TD-DFT and ab initio methods.[55,57−59] In most cases, rR intensities have been calculated by one of the methods based on (1) transform theory,[58,60] (2) short-time dynamics approximation within time-dependent formulation of Raman scattering utilizing excited-state gradients at the ground-state equilibrium geometry,[52,59] and (3) Savin's formula,[10,20b,55] which is valid in the preresonance region. To employ transform theory or Savin's furmula, one needs to know excited-state displacements that can be evaluated through excited-state geometry optimization.[55,57,58] The most important drawbacks to the use of transform theory are: (1) corresponding numerical algorithms have been developed only for the case of a single isolated electronic transition and (2) rR intensities are calculated by utilizing absorption band shape information (either the experimental one[59] or some crude approximation such aslike a simple Gaussian line[58]). It is also noteworthy that apparently

(52) Tannor, D. J.; Sundberg, J. I.; Heller, E. J. *J. Phys. Chem.* **1982**, *86*, 1822.
(53) Myers, A. B. *Chem. Rev.* **1981**, *96*, 911.
(54) Neese, F.; Solomon, E. I. *J. Am. Chem. Soc.* **1998**, *120*, 12829.
(55) Markham, L. M.; Hudson, B. S. *J. Phys. Chem.* **1996**, *100*, 2731.
(56) Bailey, S. E.; Zink, J. I.; Nelsen, F. N. *J. Am. Chem. Soc.* **2003**, *125*, 5939.
(57) Peticolas, W. L.; Rush, T., III. *J. Comput. Chem.* **1995**, *16*, 1261.
(58) Neugebauer, J.; Hess, B. A. *J. Chem. Phys.* **2004**, *120*, 11564.
(59) Szalay, P. G.; Fogarasi, G. *Chem. Phys. Lett.* **1997**, *270*, 406.
(60) Champion, P. M.; Albrecht, A. C. *J. Chem. Phys.* **1981**, *75*, 3211.

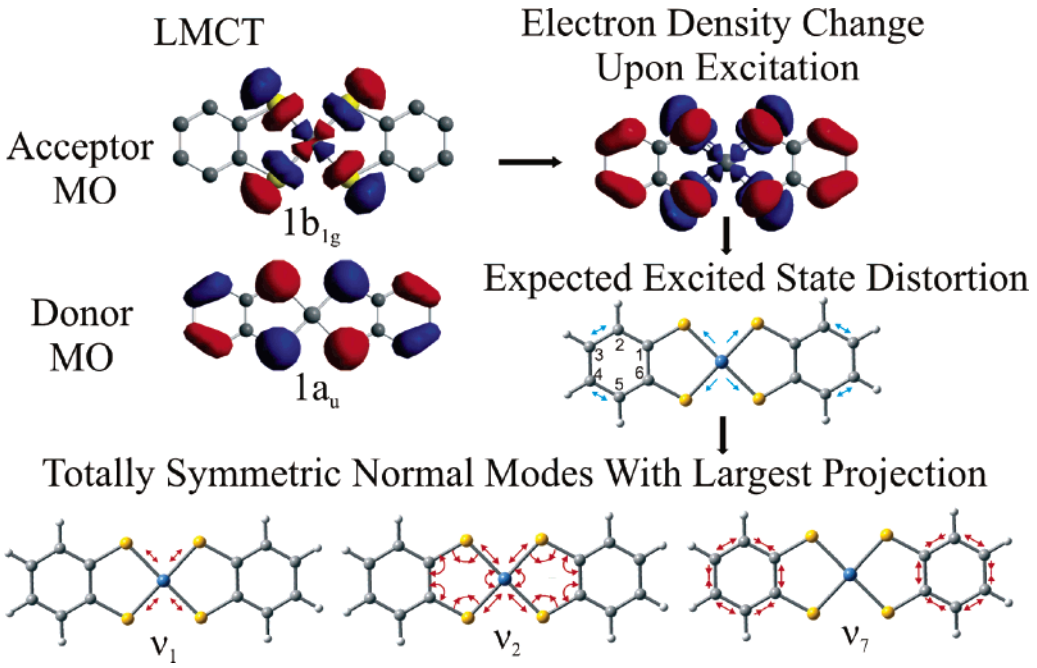

Figure 11. Normal modes with the largest excited-state displacements for the LMCT $1a_u \rightarrow 1b_{1g}$ transition of $[Ni^{II}(L)(L^{\bullet})]^{1-}$ and their relation to the nature of excitation. Donor and acceptor MOs were obtained from spin-unrestricted BP86 DFT calculations. The corresponding electronic difference density is plotted for the isodensity value of 0.0008 au (red and blue colors indicate a decrease and increase of the electronic density in the excited state, respectively). Bond length changes upon excitation are represented by outward arrows (bond elongation) and inward arrows (bond contraction).

Table 6. Experimental Fit {for $[Ni^{II}(L)(L^{\bullet})]^{1-}$ and $[Cu(L^{tBu})_2]^{1-}$} and Calculated {for $[Ni^{II}(L)(L^{\bullet})]^{1-}$ and $[Cu(L)_2]^{1-}$} Dimensionless Normal Coordinate Displacements for $1a_u \rightarrow 1b_{1g}$ Electronic Transition Obtained from the MR-DDCI2 and Spin-Unrestricted BP86 DFT Methods Using Triple-ξ (TZVP) Gaussian Bases at the Metal and Sulfur, and Split-Valence Polarized SVP Gaussian Bases for the Remaining Atoms

	$[Ni(L)_2]^{1-}$		$[Cu(L)_2]^{1-}$		
	$1a_u \rightarrow 1b_{1g}$		$1a_u \rightarrow 1b_{1g}$		
	MR-DDCI2	fit	TD-DFT	MR-DDCI2	fit[49] ($[Cu(L^{tBu})_2]^{1-}$)
Δ_1	3.34	4.3	1.64	1.67	2.15
Δ_2	2.12	1.2	1.94	1.95	$\Delta_2 = 1.23$ $\Delta_{2B} = 0.89$
Δ_3	0.22	0.76	0.26	0.41	0.70
Δ_4	0.02	—[a]	0.31	0.14	—[a]
Δ_5	0.09	—[a]	0.12	0.02	—[a]
Δ_6	0.30	0.27	0.25	0.07	—[a]
Δ_7	0.67	0.33	0.33	0.56	$\Delta_7 = 0.16$ $\Delta_{7B} = 0.18$
Δ_8	0.27	—[a]	0.02	0.06	—[a]
Δ_9	0.11	—[a]	0.05	0.05	0.16

[a] Displacements have not been fitted because the corresponding Raman bands are not unambiguously resolved or are not detected due to the close proximity of intense solvent lines. In such cases, $\{\Delta_i^I\}$ was fixed to the values obtained from the MR-DDCI2 calculation, thus resulting in negligible influence on the fitted absorption band shape and rR intensities of other modes.

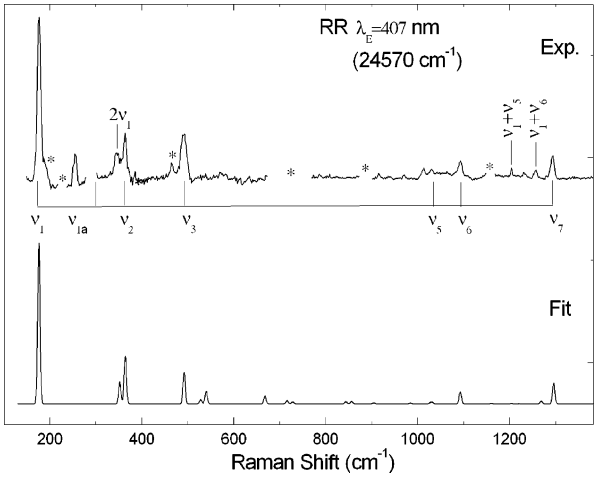

Figure 12. Experimental and simulated rR spectra for LMCT $1a_u \rightarrow 1b_{1g}$ transition of $[Ni^{II}(L)(L^{\bullet})]^{1-}$ corresponding to dimensionless normal coordinate displacements obtained from the fit (Table 6). Artifacts, solvent lines, and spectral regions with removed solvent lines are marked with asterisks. In the normal-mode representation, the length of arrows and arch lines roughly designates the relative amplitude of bond stretching and bending, respectively. Internal coordinates vibrating in antiphase are denoted by inward and outward arrows.

all previous studies refrain from the simulation of the rR intensities of overtone and combination bands. As compared to other studies, our approach has several advantages: (1) dimensionless normal coordinate displacements are evaluated in excited-state PES scan calculations rather than from excited-state geometry optimizations (the latter are difficult to perform for large molecules and frequently have large convergence problems due to curve crossings during the optimization process), (2) full-time dynamics within the time-dependent formulation of absorption band shape and rR scattering is applied, (3) corresponding simulations and fitting procedures can readily be performed in the presence of multiple electronic bands with various polarizations, and (4) rR intensities of overtone and combination bands are calculated and are taken into account in the fit, together with the fundamental bands. However, it still remains to introduce inhomogeneous broadening effects into the calculations, in particular to obtain better fits to the red edge of the absorption bands under investigation.

Taken together, we believe the present study provides detailed insight into the vibrational properties of transition metal dithiolenes, their physical origin, and their chemical implications. We hope that these insights will prove useful in further characterizing the biological Mo- and W-dithiolenes and

biologically relevant model complexes and therefore help to address the questions of whether the dithiolene ligand, in such compounds, could possibly act as a noninnocent ligand, which would certainly have significant implications for the reactivity of such sites.

Acknowledgment. We thank the Deutsche Forschungssgemeinschaft for financial support within the priority program 1137 ("Molecular Magnetism"). T.P. and K.R. gratefully acknowledge a stipend from the Max-Planck Society. Ms. Marion Stapper is gratefully acknowledged for excellent technical assistance.

Supporting Information Available: Table containing calculated frequencies of in-plane vibrations for $[M(L)_2]^{-z}$ (M = Ni, Pd, Pt, Au, Cu, Co) and their correlation throughout the compounds; UV−vis, IR, and rR spectra of $[Ni^{II}(L^{Bu})(L^{Bu\bullet})]^{-1}$, $[Pt^{II}(L^{Bu})(L^{Bu\bullet})]^{-1}$, and $[Cu^{III}(L^{Bu})_2]^{-1}$ species; figure with schematic composition of the most important totally symmetric normal modes of $[M(L)_2]^{1-}$ complexes and their benzene counterparts; table containing symmetry-adapted vibrational coordinates; figure illustrating rR enhancement mechanism for $1b_{1u} \rightarrow 2b_{2g}$ electronic transition of $[Co(L)_2]^{1-}$; figure with the fitted rR spectrum of $[Cu^{III}(L^{Bu})_2]^{-1}$ complex; complete ref 26. This material is available free of charge via the Internet at http://pubs.acs.org.

JA0578451